DUAL HIGH-VOLTAGE POWER SUPPLY FOR USE ON BOARD A CUBESAT

A Thesis
presented to
the Faculty of California Polytechnic State University,
San Luis Obispo

In Partial Fulfillment
of the Requirements for the Degree of
Master of Science in Electrical Engineering

by

Nicholas Kelly Weiser

June 2014

COMMITTEE MEMBERSHIP

TITLE:	Dual High-Voltage Power Supply for use on Board a CubeSat
AUTHOR:	Nicholas Kelly Weiser
DATE SUBMITTTED:	June 2014
COMMITTEE CHAIR:	Dr. Taufik Professor of Electrical Engineering
COMMITTEE MEMBER:	Dr. Dale Dolan Professor of Electrical Engineering
COMMITTEE MEMBER:	Dr. Jordi Puig-Suari Professor of Aerospace Engineering

ABSTRACT

Dual High-Voltage Power Supply for use on Board a CubeSat

Nicholas Kelly Weiser

Since their conception in 1999, CubeSats have come and gone a long way. The first few that went into space were more of a “proof of concept,” and were more focused on sending simple data and photographs back to Earth. Since then, vast improvements have been made by over 40 universities and private firms, and now CubeSats are beginning to look towards interplanetary travel. These small satellites could provide a cost effective means of exploring the galaxy, using off the shelf components and piggy-backing on other launch vehicles with more expensive payloads. However, CubeSats are traditionally launched into Low Earth Orbit (LEO), and if an interplanetary satellite is to go anywhere from there, it will need a propulsion system. This thesis project’s main goal will be to investigate the possibility and capability of an Ion-Spray propulsion system. Several problems are to be tackled in this project: how to take a 9 V supply and boost it to a maximum potential difference of 5,000 V, all while minimizing the noise and testing the feasibility of such a system being flown on board a CubeSat.

Keywords: Power electronics, CubeSat, high voltage, SLR

ACKNOWLEDGMENTS

Without the people detailed below, I would absolutely not be in the position that I am today. I owe each and every one of them, as well as countless others, my gratitude forever.

I would like to thank my family for their support, love, and encouragement, from the application to Cal Poly right up until graduation this June. Thanks for encouraging me repeatedly to shoot big, and helping me take the shots! I would also like to thank my sister, since she blazed the steep trail towards the engineering realm. Without her, maybe I would be a good for nothing scientist or doctor. Regarding future doctors, I also owe many thanks to Casey Pagan, who has brought me so much joy and support throughout my entire academic career. Of course, I am grateful to have met and spent countless enjoyable weekends with Jean Gordon, whose garden I hope continues to flourish.

I could not have gone anywhere without the expertise of my advisor Dr. Taufik, who through his great excitement during lectures sparked my interest in the Power Electronics realm. DC-DC converters still seem like magic to me, which is a sense of awe that Dr. Taufik maintained. Finally, I cannot express enough gratitude towards the PolySat and CubeSat labs on campus. Dr. Puig-Suari, Dr. Bellardo, and of course all of the staff and students, current and former, opened my eyes to the possibility of working in the aerospace industry. Working on these star-bound projects put a twinkle in my eye and heart, and that twinkle will never fade.

Table of Contents

List of Tables

List of Figures

1. Introduction

1.1 CubeSat Background

CubeSats are small satellites that are highly constrained in volume and mass. A typical 1 unit (1U) CubeSat is 10 cm x 10 cm x 10 cm, and weighs up to 1300 grams (see Figure 1.1). Since the definition of this form-factor in 1999 by professors Jordi Puig-Suari (Cal Poly) and Bob Twiggs (Stanford), CubeSats have grown from a novel concept to a small industry. Despite the size and mass restrictions, over 50 universities and corporations have been able to demonstrate the surprising capabilities offered by this platform. This success has been driven by numerous advances in technology in the consumer electronics market, as well as the development of the Poly Pico-Orbital Deployer, or PPOD (see Figure 1.2). The PPOD is a jack-in-the-box style system that can fit three 1U satellites, or an equivalent configuration of 1.5 U, 2U, and 3U size spacecraft. Partnership with NASA and different launch vehicle developers has allowed these groups to develop and fly various sensors such as cameras, ion-spectrometers, solar-angle sensors, star trackers, and even micro-biological laboratories, to name a few.

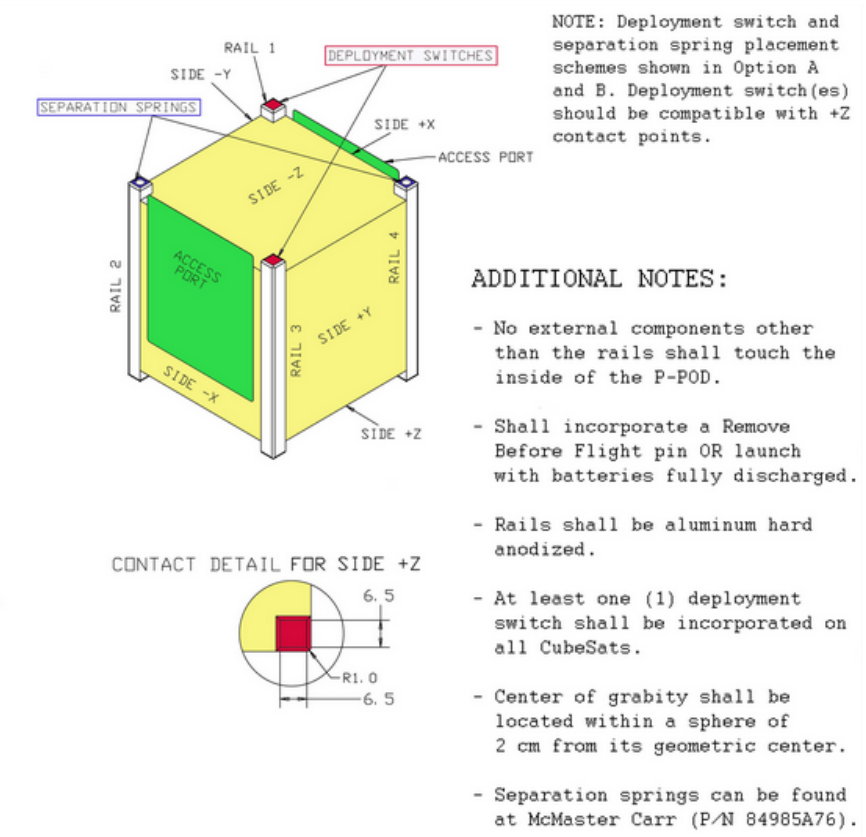

Figure 1.1: CubeSat specification diagram [1].

Figure 1.2: The PPOD, through which CubeSats are deployed [2].

1.2 CubeSat Team Lifecycle

Most universities begin their small satellite teams by developing a relatively simple CubeSat which demonstrates communication capabilities from low earth orbit (LEO), as well as the demonstration of some form of new technology. In the case of CP1, Cal Poly's first satellite, the main payload was a sun sensor developed by Optical Energy Technologies. Once a team has demonstrated this level of success, a more complex mission will be proposed, developed and flown. Since the PolySat program's inception in 1999 at Cal Poly, multiple generations of students have improved the bus, which is typically defined as the core system of the satellite, not including the payload. The bus consists of the command and data handling, avionics, power generation, and communication subsystems. Due to this improvement, the PolySat team has been able to shrink the bus volume to allow roughly 75% of a 1U to be dedicated solely to the payload. This allows for the incorporation of substantially more complex spacecraft that can control its attitude and determination, deploy expandable solar panels or antennas, and incorporate larger payloads. PolySat's tenth satellite, ExoCube, is an example of such improvements. ExoCube is a 3U that will have deployable gravity gradient booms, a reaction wheel for pointing accuracy, and nearly 1.5U of space for an ion-spectrometer developed by NASA–Goddard.

1.3 Single CubeSat Lifecycle

Teams of students typically begin a project by submitting a proposal for a project in response to a call for papers, published by organizations such as NASA or the National Science Foundation. These calls for papers will express interest in specific technology demonstrations or capabilities that can only be proven in low earth orbit and beyond.

Once a team is selected and funding for a project is approved, they then will embark on a 1-4 year long journey of design, development, testing and verification of the initial goals mission objectives. Due to the short mission timeline, students have the unique opportunity to complete a project from concept to launch. There are few situations in which students can gain hands-on experience not only developing, but proving flight quality hardware in such an academic environment.

Once a satellite has been approved for flight by completing several design reviews and environmental testing, the developing teams bring their system to the Cal Poly campus for final integration into a PPOD. The PPOD is then delivered to the launch vehicle, which launches and deploys the primary payload (typically a multi-million dollar mission for governmental organizations, communications companies, or research groups), the CubeSats are released from the PPOD, thus beginning their missions. Students then complete the mission from the ground by gathering the necessary data generated by their satellites, and subsequently analyzing the results, ultimately drawing conclusions about the effectiveness of their payload and system as a whole. The students then take these results to their customers (the payload developers), and present these results to the CubeSat community during the annual workshop, held in April on the Cal Poly Campus.

1.4 Progress as an Industry

When cellular telephones were first introduced to the world, they were bulky and served the sole purpose of voice communication. Today, we have cell phones that can take pictures, navigate users to their favorite restaurants, browse the web, play music, and countless other features. The CubeSat industry has seen a similar growth, due to the repeatedly surprising capability to provide impressive results in highly integrated

packages. Much like cell phone consumers, the aerospace industry has found itself yearning for more from their products. Because CubeSats are not the primary payload of a launch vehicle, developers find themselves limited to specific orbits based on the requirements of the primary payload's mission. If, for instance, a CubeSat's mission is to measure ion and neutral densities in the exosphere, but the launch vehicle is only capable of deploying the satellite into the upper ionosphere, then it would be convenient to be able to change that orbit by some means of propulsion device. Conversely, if a satellite finds itself deployed into a substantially higher altitude than its team can support, then declining in elevation would be necessary. Currently, deorbiting has been proven by satellites such as Nanosail-D, which deployed a solar sail, which increased the drag coefficient, forcing the unit to return to earth in a much shorter time span than without such a sail. Passive deorbiting units such as Nanosail-D are a good option for systems that must return closer to Earth, but changing orbit in the opposite direction is currently an unproven system. To combat this, micro-propulsion systems are being developed to be tested aboard CubeSats. Due to the risk-averse nature of launch vehicle providers, as well as the primary payloads that they support, such active systems are typically not allowed on board the same launch. Despite these challenges, the aerospace industry is pushing towards developing CubeSats that, like cell phones, will redefine what was previously considered possible. For instance, in February 2014, NASA published a request for information regarding a centennial challenge. In this RFI, NASA requested input from the CubeSat community on the subject of what exactly the centennial challenge should be, but defining two main goals: development of long distance (beyond low earth orbit) communication capabilities, and propulsion systems for CubeSats.

2. Background

2.1 Spacecraft Propulsion Systems

2.1.1 Passive Propulsion Systems

Currently, there exist two types of passive propulsion systems, which do not use expendable fuel sources to change their altitudes. The first is a tether system, where a long cable is deployed from the spacecraft, examples of which are shown in Figures 2.1 and 2.3. Currently, tethers have only been implemented in the CubeSat community as a means of minimizing de-orbiting time than without deploying the tether, as shown in Figure 2.2. With this method, de-orbiting is achieved by increasing the overall surface area of the satellite, which in turn increases the amount of drag and slows the system down. Conversely, it is theoretically possible to increase orbital altitude by implementing a conductive tether, which can be used to generate thrust against the Earth's magnetic field, and repel the systems into a higher orbit. The second system uses a sail mechanism, which can be used to decrease orbital lifetime in the same manner by increasing drag. Though it has yet to be proven, orbital altitude may be increased by using solar radiation to push the satellite away from the Earth. Such a system will be attempted by the LightSail mission, which will deploy a 31 square meter sail after deployment [3]. An example of such a system is shown in Figure 2.4.These two systems are lightweight and relatively simple to control, but they come at the great disadvantage of lower amounts of control.

Figure 2.1: Naval Research Laboratories TEPCE CubeSat tether testing during a free-fall test [4].

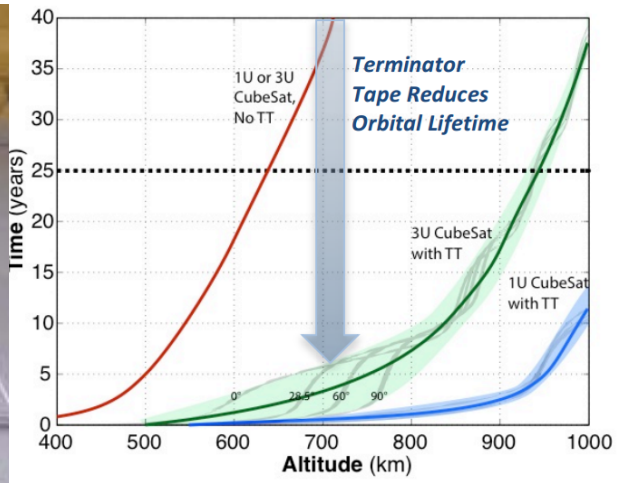

Figure 2.2: Graph showing the greatly reduced orbital lifetime resulting from deploying a tether [5].

:

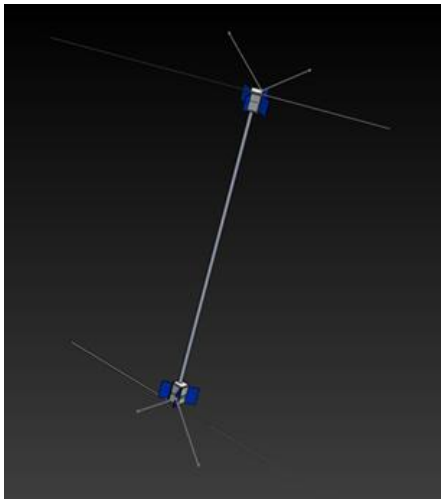

Figure 2.3: Naval Postgraduate School's TetherSat 1 &2, coupled by a tether [6].

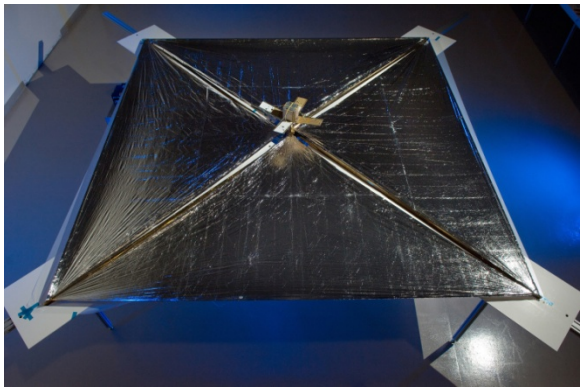

Figure 2.4: NanoSail-D with a fully deployed solar sail [7].

2.1.2 Chemical Propulsion Systems

Chemical propulsion systems generate force by fuel expulsion, resulting in acceleration according to Newton's third law. Hydrazine, hydrogen peroxide, and cold gas thrusters are all examples of such systems, and are shown in Figures 2.5 and 2.6. They offer the

advantage of larger specific impulse, meaning that a larger change in velocity can be exerted. Disadvantages of chemical propulsion include increased power consumption and mass, two aspects crucial to a CubeSat [8]. Another disadvantage is that these options often require pressurized vessels, as in the case of the cold gas and hydrogen peroxide thrusters. From the eyes of the launch provider, pressure vessels are considered a threat to the primary payload, because in the event of a failure of the vessel to maintain pressure, debris could be generated during the rocket's ascent which could then damage the primary payload. Hydrazine systems are also highly toxic, and considered to be a range safety issue.

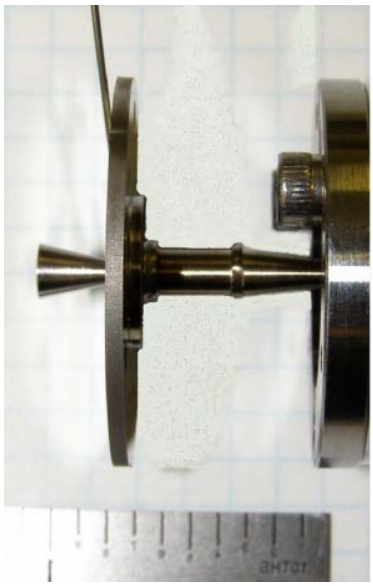

Figure 2.5: Hydrazine thruster system [9] .

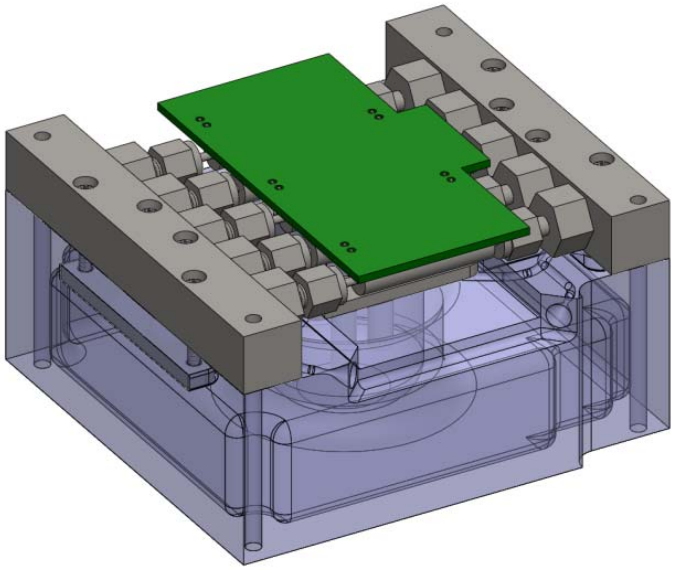

Figure 2.6: Cold Gas thruster system to be implemented on NASA's INSPIRE mission [10].

2.1.3 Electric Propulsion Systems

Electric propulsion systems operate similar to chemical propulsion systems, where a force is generated to propel the spacecraft due to mass expulsion.The key difference with these systems is that instead of using energy stored in the propellant, electrical energy is

used to actuate the propellant. Electric propulsion options include pulsed plasma thrusters (PPT), vacuum arc thrusters, ion engines, Hall effect thrusters, and electrospray thrusters. While electric thrusters do require volume and mass for the propellant, smaller amounts can be used because these systems generate high velocity particles, thus providing the same average amount of thrust for lower amounts of fuel. The major disadvantage is presented in the power supply, specifically because large capacitor banks are required to generate high voltage and deliver the necessary power. Examples of electric propulsion systems are seen in Figures 2.7 and 2.8. Unlike chemical propulsion options, which require large valves, storage tanks, and pressure vessels, electric propulsion systems can be implemented easily into a small form factor such as a CubeSat. NASA-JPL is in the process of developing an electrospray sensor meant to be implemented on board a CubeSat. The size is roughly that of a sugar cube, and similar to other such devices, requires a large potential difference to actuate. This thesis will investigate the development and testing of such a power supply.

Figure 2.7: ST-7 Electrospray thruster [11] .

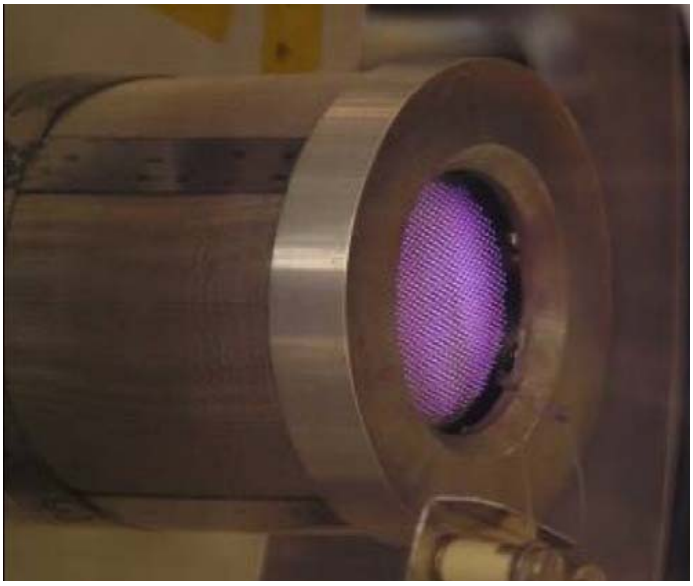

Figure 2.8: MiXI Ion Thruster engine in operation. [12].

2.2 Typical High Voltage Architecture: Non-Aerospace Applications

Outside of the aerospace industry, many of the concerns faced in the CubeSat realm are avoided. Specifically, there are fewer constraints on mass and volume. However, it is usually expected that the system will be capable of producing much higher power. As mentioned, the CubeSat system will only be capable of a few (<10) watts, whereas a high voltage system on Earth will consume power in the kilowatt range. Medical equipment such as X-ray machines [11] [12] and older video display systems [13] require such high voltage. In these types of systems, it is typical to implement a bridge driving inverter topology, followed by a high ratio step up transformer, then followed finally by rectifiers to convert the overall system to DC voltages [14]. An example of this can be seen in Figure 2.9. Adding in series resonant components such as inductors and capacitors allows for the addition of features such as zero voltage or zero current switching, which adds the advantage of decreased switching losses, resulting in higher overall efficiency. In the power electronics realm, it is generally acceptable to use simple double order systems such as series loaded or parallel loaded resonant converters. Increasing the order of the resonant load allows for higher frequency operation, which results in a decrease in overall component and system mass and volume. The disadvantage to increasing the order of the resonant load is that the system is more sensitive to noise and manufacturing errors present in the components themselves. Examples of higher order systems can be seen in Figures 2.10 and 2.11.

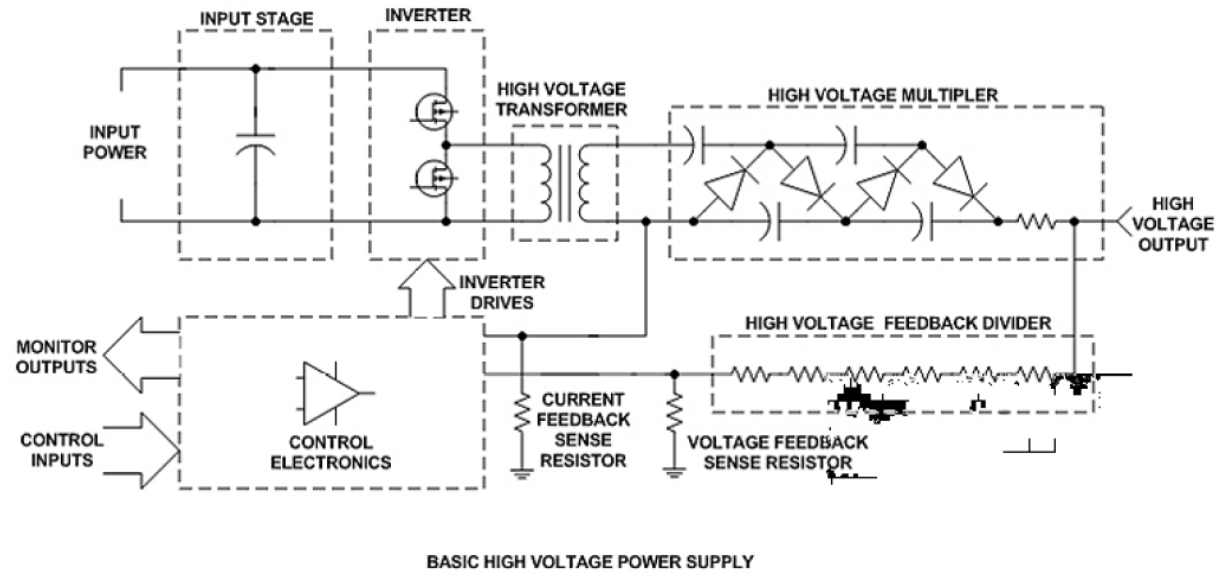

Figure 2.9: Block diagram showing a typical high voltage schematic [16].

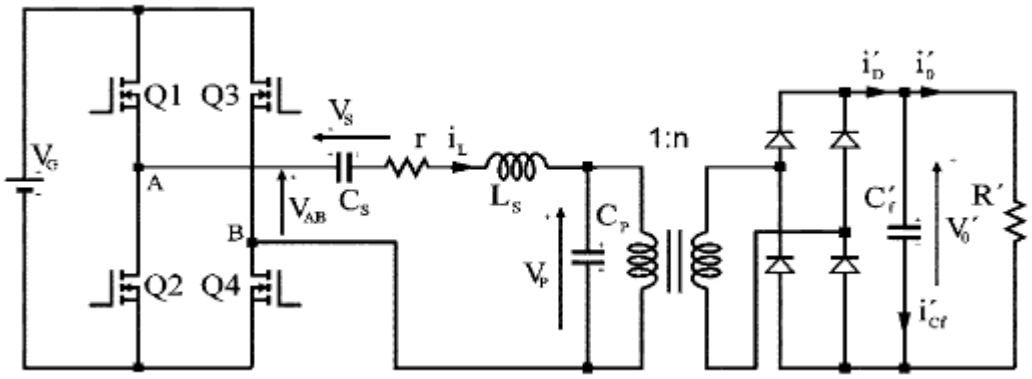

Figure 2.10: High voltage power supply for X-Ray tube, implementing parallel resonant converter LCC topology [14].

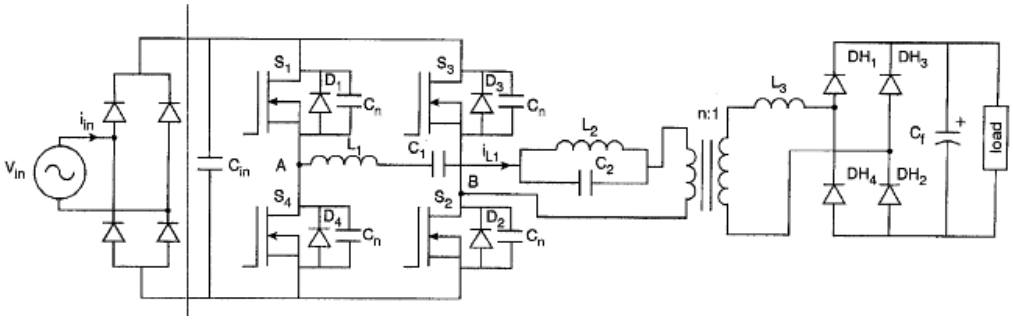

Figure 2.11: High order series resonant converter topology [17].

2.3 Topology Refinement

In designing a high voltage power supply for an electrospray thruster for a CubeSat class spacecraft, all possible topologies must be considered. Due to the high voltage requirements, there are two things that are considered non-negotiable: first, there must be a high ratio step-up transformer. Second, it must be followed by voltage multipliers for output rectification and conditioning. For the sake of simplicity and reliability, multiphasing and interleaved topologies will not be considered. In the cases where soft switching is an option, it must be applied. The term soft-switching refers to a switching method used to turn on and turn off a switch while the switch voltage or current is at zero value. This is in contrast with PWM where a switch is turned on while its voltage is high, and turned off while its current is high, thus incurring significant switching loss which worsens with increased switching frequency. Soft switching is crucial, since it does not generate large amounts of electromagnetic interference (EMI), which at high enough levels can damage components or prevent entire subsystems from functioning properly. In most cases, soft-switching can be implemented by running the converter in discontinuous conduction mode (DCM). A trade study between four different topologies is shown below in Figures 2.12 – 2.15, with a summary of the results in Table 2-1.

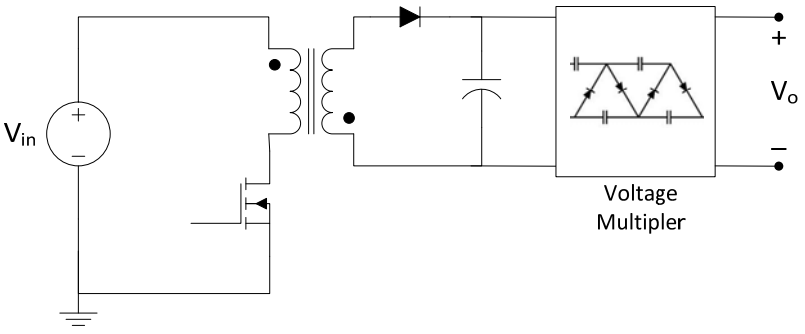

Figure 2.12: Power stage of Flyback with Voltage Multiplier

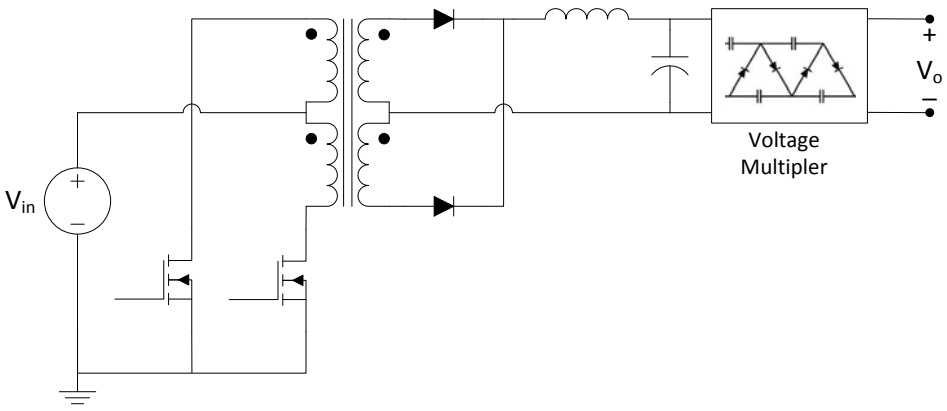

Figure 2.13: Power stage of Push-Pull with Voltage Multiplier

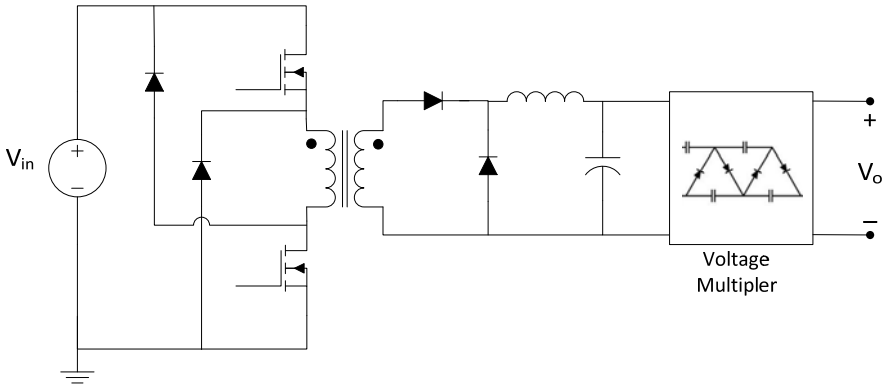

Figure 2.14: Power stage of Two-switch Forward with Voltage Multiplier

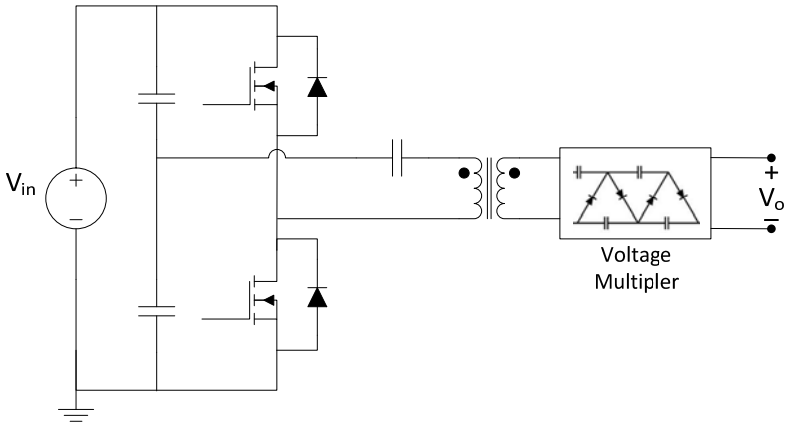

Figure 2.15: Power stage of Series-Loaded Resonant with Voltage Multiplier

Table 2.1: Candidate topologies with their advantages and disadvantages

Topology	Advantages	Disadvantages
Flyback DCM	• Simple • Low part count • Low cost • Minimized transformer weight • Improved output ripple	• Increased cost and losses due to voltage multiplier parts • Slow transient response
Push-Pull	• Clean input and output ripple • Low noise	• Large and heavy due to 4-winding transformer and an output inductor • Many components • Costly • Limited in duty-cycle
Two-switch Forward	• Inherent clamping of leakage inductance spike	• Requires two magnetic components (a 2-winding transformer, an output inductor) • Limited in duty-cycle
Series-Loaded Resonant DCM	• Soft-switching for increased efficiency and low noise • Employs a 2-winding transformer (like Flyback) • Takes advantage of transformer's leakage inductance • Inherent short circuit protection • Able to use slow diodes	• More complex controller • High switch current rating

Observing the trade-offs described in Table 2.1, the most suitable topology for the dual high-voltage power supply for the CubeSat is found to be the Series-Loaded Resonant (SLR) topology, for the following reasons:

1. Requires only one magnetic component: a transformer with two windings, thus minimizing its overall weight, size, and cost.
2. Does not have the issue with transformer's leakage inductance which is known to produce leakage spikes, as with Flyback. The leakage spike is an undesired effect that imposes high voltage spikes across the main switch on the primary side and diode on the secondary side of the transformer. SLR makes use of the leakage inductance in series with the primary winding inductance to produce a resonant frequency used for soft-switching.

3. Is a low-noise converter since it employs soft-switching in DCM.
4. Has inherent short circuit protection on its output when operated in DCM.
5. Allows flexibility in the choice of switch (may use semicontrollable switch) as well as diodes (may use PN diodes).
6. Uses a fixed conduction time of the switch while still providing a wide range of duty cycles.

For the reasons described above, as well as the heritage that such a topology has within the realm of ground-based converters, the SLR topology will be developed to provide power for the previously discussed electrospray thruster developed by NASA-JPL.

3. Design Requirements

Figure 3.1 illustrates the overall system requirements for the proposed power supply, with the results being tabulated in Tables 3.1 and 3.2

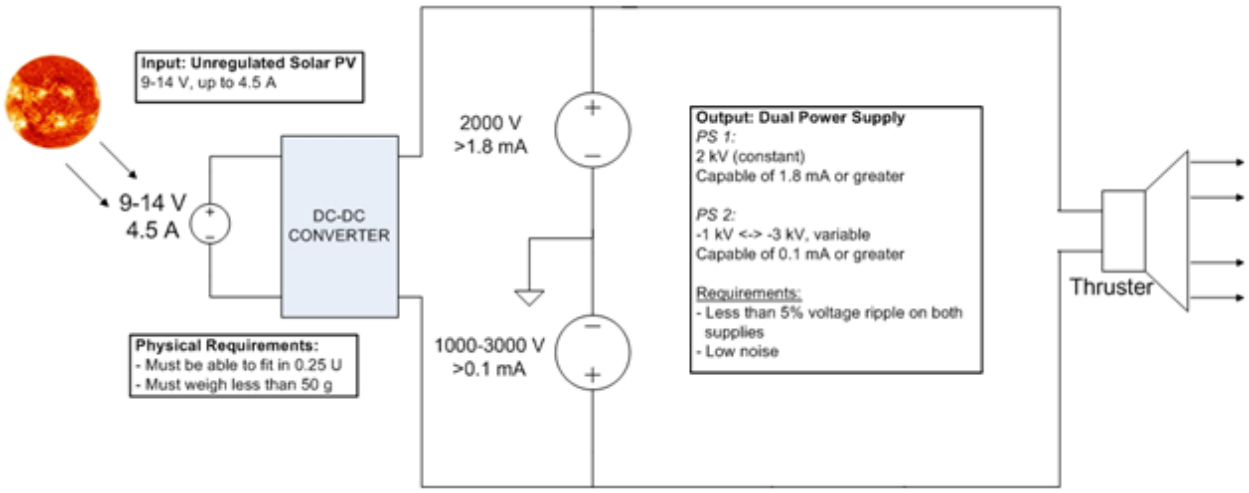

Figure 3.1: Block diagram of the proposed power supply, with requirements listed.

3.1 Source Capabilities

The power system on board a CubeSat is typically comprised of solar cells in parallel with a Lithium-Ion battery bank. The batteries allow the spacecraft to continue operations during eclipse periods. The batteries can be conFigured as a parallel bank, series, or any combination of the two. For this mission several batteries used in the combination of parallel and series were to be implemented. Because the nominal operating voltage of Lithium-Ion cells lies within 3.0 V-4.2 V, the series (triple) combination results in an overall bus voltage of 9 V-12 V. To add margin, peaks up to 14 V must also be tolerable. The storage system is capable of delivering up to 4.5 A.

3.2 Primary Converter Requirements

The nature of an ion-spray thruster requires large voltage potentials in order to actuate

and engage the ions. The particular thruster under consideration requires a minimum of 3000 V from anode to cathode. This limit can be increased, with the result being an increase in thrust, due to higher velocity of the ions being propelled. JPL required a maximum potential difference range up to 5000 V. Specifically, one constant 2000 V rail is required, from which at least 1.8 mA must be delivered to the thruster. In addition, another negative rail must be provided, which can vary from -1000 V to -3000 V while delivering at least 0.1 mA. Both converters must also contain no more than 5% ripple.

3.3 Secondary Converter Requirements

In order to accommodate the supply in the form factor that a 3 U CubeSat provides, several secondary requirements were imposed onto the project. The maximum mass of the unit must weigh no more than 50 grams, and occupy no more than 0.25 U (2.5 cm x 10 cm x 10 cm). In order to determine the amount of thrust being generated, output voltage sensing on both rails is crucial. Lastly, since these spacecraft rely on RF communication, low EMI is also desirable.

Table 3.1: Primary Requirements definitions set by NASA-JPL.

Primary Requirement	Condition
Source Input Voltage	9-14 V
Source Input Current	4.5 A
Power Supply 1 Output Voltage	2000 V (constant)
Power Supply 1 Output Current	> 1.8 mA
Power Supply 2 Output Voltage	-1000 ↔ -3000 V (variable)
Power Supply 2 Output Current	> 0.1 mA
Output voltage ripple (both)	< 5% ripple

Table 3.2: Secondary Requirements definitions set by NASA-JPL.

Secondary Requirement	Condition
Overall system mass	50 grams maximum
Overall system volume	0.25 U maximum (2.5 cm x 10 cm x 10 cm)
EMI	Low

4. Design and Simulation

Using the requirements as defined in Chapter 3 and implementing the Series Loaded Resonant topology as discussed in Chapter 2, specific component sizes can be defined in an ideal case. The system will operate in the discontinuous conduction mode, resulting in higher efficiency by decreasing switching losses, as well as generating lower EMI due to decreasing the sudden current spikes that result from hard switching topologies. Due to the constant-on nature of the SLR topology, the negative rail can be varied by increasing or decreasing the switching frequency. The following Equations detail the component sizing process for this converter based on the requirements discussed in Chapter 3. Assumptions made during these calculations include complete ideality, and that a controller can operate at a maximum of 500 kHz. Lastly, it is assumed that 95% margin will be necessary to force the system to operate in discontinuous conduction mode.

4.1 Design

The following section will detail the setup and design calculations required to build a high voltage power supply based on the SLR topology.

4.1.1 Initial Parameter Definitions

Based on Table 3.1, the initial parameters are defined below.

Input Capabilities:

$$Vin_{minimum} = 9\ V \qquad Vin_{maxmimum} = 14\ V$$

Output Requirements:

$$Vout_{positive} = 2000\ V \qquad Iout_{positive} => 1.8\ mA$$

$$Vout_{negative\ minimum} = -1000\ V$$

$$Vout_{negative\ maximum} = -3000\ V \qquad Iout_{negative} => 0.1\ mA$$

In order to guarantee the converter's operation at the specified currents shown above, it was necessary to design the system to provide those values at minimum. For this reason, the output current and power requirements were designed to be 5 times larger than the minimum values, as seen in Equations 4.1 to 4.5 below.

Output current requirements:

$$Iout_{positivemaximum} = 5 * Iout_{positive} \quad (4.1) \qquad Iout_{negativemaximum} = 5 * Iout_{negative} \quad (4.2)$$

Positive rail maximum power output:

$$Pout_{positivemaximum} = Vout_{positive} * Iout_{positivemaximum} = 18\ W \quad (4\text{-}3)$$

Negative rail maximum and minimum power outputs:

$$Pout_{negativemaximum} = Vout_{negativemaximum} * Iout_{negativemaximum} = 1.5\ W \quad (4.4)$$

$$Pout_{negativeminimum} = Vout_{negativeminimum} * Iout_{negativemaximum} = 0.5\ W \quad (4.5)$$

4.1.2 Postive Rail Converter Design

As mentioned above, for the sake of initial comoponent sizing, it is assumed that a controller can be found capable of providing the necessary switching signals at 500 kHz. It is also assumed that in order to guarantee operation in DCM, 95% margin will be imposed on the switching frequency. These details can be seen below in Equations 4.6-4.10. Resonant component sizing and selection can be seen in Equations 4.11-4.14.

Switching frequency definition:

$$f_{sw} = 500\ kHz \rightarrow \omega_{sw} = 2\pi f_{sw} = 3.142 * 10^6\ \frac{rad}{sec} \tag{4.6}$$

Switching Period and Margin definition:

DCM operation occurs when switching frequency is less than ½ Resonant frequency. Adding this 95% margin allows for component values to vary slightly within manufacturing tolerances and still maintain DCM.

$$Margin_{\%} = 0.95 \tag{4.7}$$

$$T_{sw} = \frac{1}{f_{sw}} = 2\mu s \tag{4.8}$$

$$T_{resonant} = Margin_{\%} * \frac{T_{sw}}{2} = 0.95\mu s \tag{4.9}$$

$$f_{resonant} = \frac{1}{T_{resonant}} = 1.053\ MHz \rightarrow \omega_{resonant} = 2\pi f_{resonant} = 6.614 * 10^6\ \frac{rad}{sec} \tag{4.10}$$

Resonant Component Sizing:

Resonant components must be selected based on Equations 4.6 and 4.10. Because it is commercially available in multiple sizes and power ratings, a 1 nF capacitor is selected for the sake of convenience. As seen below in Equations 4.11- 4.13, this also results in a conveniently sized resonant inductor value. These values are easily modified to accommodate different (lower or higher frequency) operating conditions, but the values shown below are chosen to be as such for initial component sizing purposes. Choosing a slightly larger capacitor or inductor value maintains DCM and also allows for the implementation of a more commercially available value, as seen with Equation 4.14.

$$f_{resonant} = \frac{1}{2\pi\sqrt{C_{resonant} * L_{resonant}}} \tag{4.11}$$

$$C_{resonant} = 1\ nF \tag{4.12}$$

$$L_{resonantminimum} = \frac{1}{C_{resonant} * (2\pi f_{resonant})^2} = 22.861\ \mu H \tag{4.13}$$

$$L_{resonant} = 25\mu H \tag{4.14}$$

Output Voltage and Turns Ratio Calculations:

Equations 4.15-4.22 detail the sizing process for the transformer. Equations 4.15-4.17 provide the necessary variables based on Equations 4.12 and 4.14 to compute Equations 4.18 and 4.19. Equations 4.15 and 4.18-4.19 are derived from the sinusoidal method to estimate output voltages for a "standard" bridge rectified SLR converter. These two Equations provide a rough estimate for the input to the transformer. As seen in Equation 4.20, it is assumed that 4 voltage multiplication stages will be implemented. Knowing the maximum output voltage, as well as the maximum and minimum inputs to the transformer, it is possible to work backwards and determine the turns ratio necessary to achieve the maximum output voltages, as seen in Equations 4.19-4.22.

$$R_{outpositivefullload} = \frac{{V_{outpositive}}^2}{Pout_{positivemaximum}} = 222\ k\Omega$$
$$R_{epositivefullload} = \left(\frac{8}{\pi^2}\right) * R_{outpositivefullload} = 0.18\ \text{M}\Omega \tag{4.15}$$

$$X_L = \omega_{sw} * L_{resonant} = 78.54\ \Omega \tag{4.16}$$

$$X_C = \frac{1}{\omega_{sw} * C_{resonant}} = 318.31\ \Omega \tag{4.17}$$

$$V_{oresonantloadmax} = Vin_{maximum}\left[\frac{1}{\sqrt{1 + \left(\frac{X_L - X_C}{Re_{pos}}\right)^2}}\right] = 14\ V \tag{4.18}$$

$$V_{oPosResonantloadmin} = Vin_{minimum}\left[\frac{1}{\sqrt{1+\left(\frac{X_L - X_C}{Re_{pos}}\right)^2}}\right] = 9\ V \tag{4.19}$$

$$Mult_{stages} = 4 \tag{4.20}$$

$$V_{osecpos} = \frac{Vout_{positive}}{2^{Mult_{stages}}} = 125\ V \tag{4.21}$$

$$Ratio_{positive} = ceiling\left(\frac{V_{osecpos}}{V_{oPosResonantloadmin}}\right) = 14 \tag{4.22}$$

Basic Component Sizing:

In order to accurately search for components to implement in hardware, it is necessary to determine the voltage and current requirements for each component. Equations 4.23-4.27 detail this process. In order to determine the switch current rating, an assumed 80% efficiency is incorporated for the sake of contingency. This is seen in Equation 4.24.Because the freewheeling diodes are in parallel with the switches, they must meet the same voltage and current requirements as the switches, as shown in Equation 4.25. The resonant capacitor must be able to tolerate the full input voltage maximum, as shown in Figure 4.1. Finally, the resonant inductor current is derived in Equation 4.27, based on Equation 4.26. Because there are no initial conditions imposed on the inductor, both the I_{Lo} and V_{co} terms equate to 0, leading the result shown in Equation 4.27.

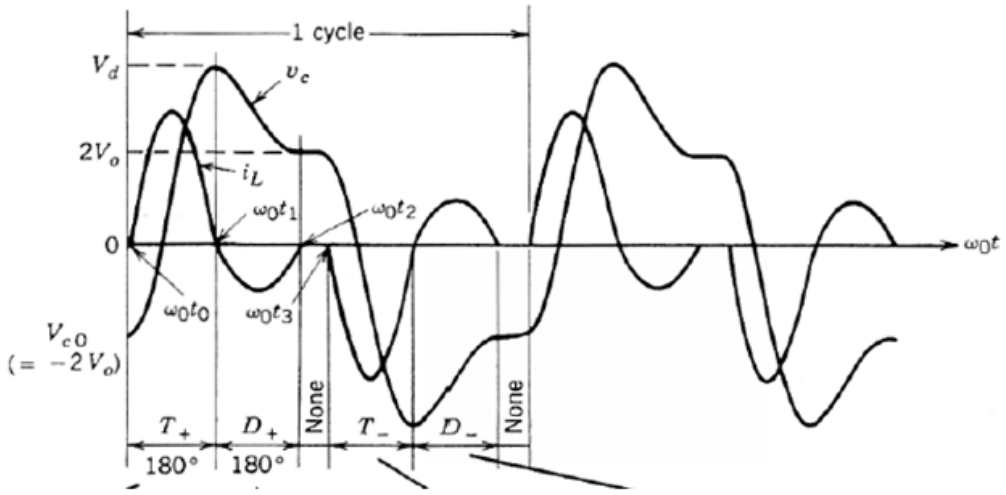

Figure 4.1: Graph showing two periods of resonant capacitor voltage and resonant inductor current.

$$V_{SW} = 2 * Vin_{maximum} = 28\ V \tag{4.23}$$

$$I_{SW} = \frac{\frac{Pout_{positivemaximum}}{0.8}}{Vin_{minimum}} = 2.5\ A \tag{4.24}$$

$$V_{ResonantCapacitor} = Vin_{maximum} = 14\ V \tag{4.25}$$

$$I_L(t) = I_{Lo}\cos\omega_o t + \frac{V_d - V_{Co}}{Z_o}\sin\omega_o t \tag{4.26}$$

$$I_{Lpeak} = \frac{Vin_{maximum}}{\sqrt{\frac{L_{resonant}}{C_{resonant}}}} = 0.089\ A \tag{4.27}$$

4.1.3 Negative Rail Converter Design

The design process for the negative rail converter is essentially the same. In order to create a simple, reliable system, the same switching frequency and resonant component values are used. For this reason, as well as the use of very large equivalent resistances (as seen in Equations 4.28 and 4.29), the input to the transformer is the same value as seen in Equations 4.18-4.19. Because the output of the negative rail is to be larger, the only

parameter that needs to be derived in this case is now the turns ratio of the transformer. This can be seen in Equations 4.30-4.31.

$$R_{outnegativeminimum} = \frac{V_{outnegativeminimum}{}^{2}}{Pout_{negativeminimum}} = 2\ M\Omega$$
$$R_{enegativeminimum} = \left(\frac{8}{\pi^2}\right) * R_{outnegativeminimum} = 1.621\ \text{M}\Omega \quad \textbf{(4.28)}$$

$$R_{outnegativemaximum} = \frac{V_{outnegativemaximum}{}^{2}}{Pout_{negativemaximum}} = 6\ M\Omega$$
$$R_{enegativeminimum} = \left(\frac{8}{\pi^2}\right) * R_{outnegativeminimum} = 4.683\ \text{M}\Omega \quad \textbf{(4.29)}$$

$$V_{osecneg} = \frac{Vout_{negativemaximum}}{2^{Mult_{stages}}} = 187.5\ V \quad \textbf{(4.30)}$$

$$Ratio_{positive} = ceiling\left(\frac{V_{osecpos}}{V_{oPosResonantloadmin}}\right) = 21 \quad \textbf{(4.31)}$$

Finally, because the output power of the positive converter is substantially higher than that of the negative converter, as well as the use of the same resonant components, all initial component sizing values should be left as is. This will generate a simple, consistent converter that should operate reliably.

4.2 Simulation

Using the calculated values from section 4.1, a simulation was completed using OrCAD PSpice. These simulations were completed assuming the most ideal situations. The component Sbreak is used as a model of the MOSFETs, with an on resistance 10 mΩ. The component Dbreak is used as a model of the diodes. Due to the non-sinusoidal nature of the voltage waveforms across the inductor for an SLR operating in DCM, the transformer is being modeled as a VCVS with gain of 24 (up from the calculated 14) on

the positive rail and 35 on the negative rail (up from the calculated 21). This large increase is caused by the initial calculations shown in Equation 4.18-4.19, which assumed that the output of the SLR topology would be met with a full-bridge rectifier. In this case, the bridge rectifier has been replaced with voltage multiplication stages, which only act as half bridge rectifiers. The increase is also a result from incorporating the small losses in the Sbreak models, as well as voltage drops across Dbreak. The first simulation completed was with both converters operating at the maximum switching frequency of 500 kHz. Figures 4.2 and 4.3 show the circuits implemented in PSpice.

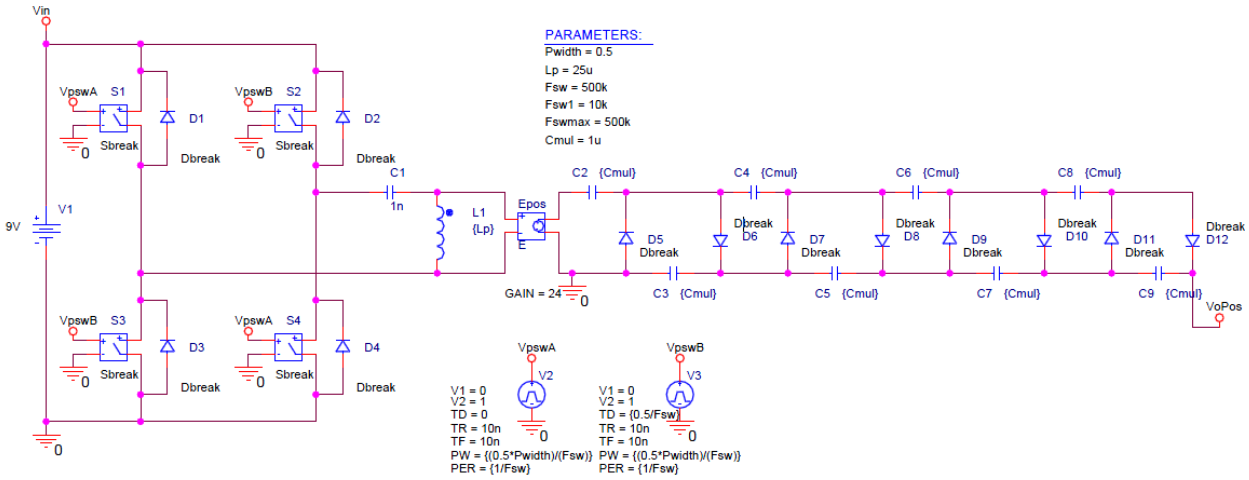

Figure 4.2: Positive rail conversion.

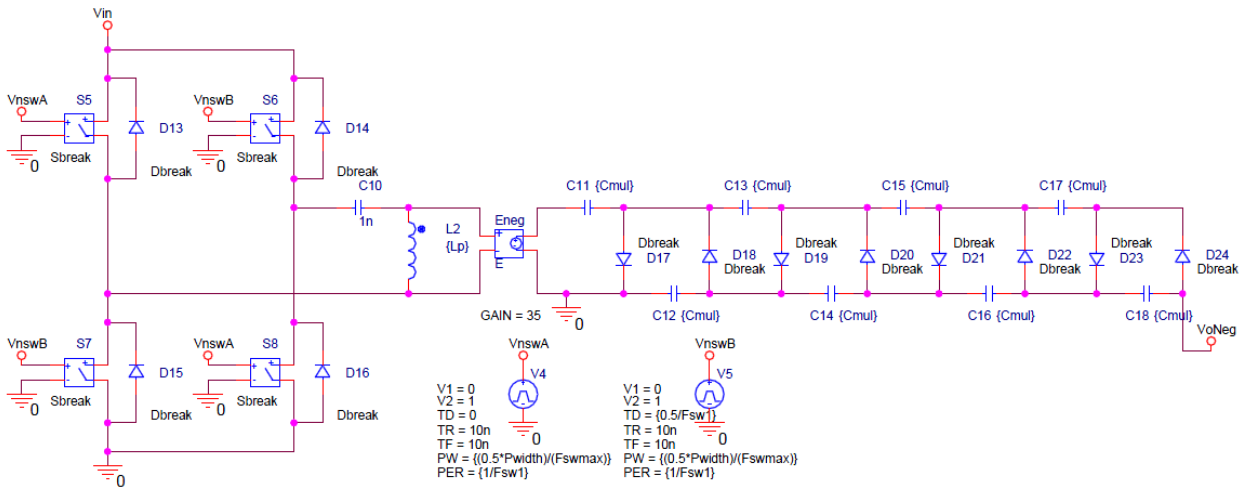

Figure 4.3: Negative rail conversion.

Below in Figure 4.4, the maximum output voltage conditions are demonstrated at the assumed maximum frequency of 500 kHz. Figure 4.5 shows that at 500 kHz, both rails are operating in boundary conduction mode (BCM) as designed. In Figure 4.6, the switching frequency of the negative rail is lowered to 100 kHz, demonstrating separation of the resonant current periods, thus allowing for variable output voltage.

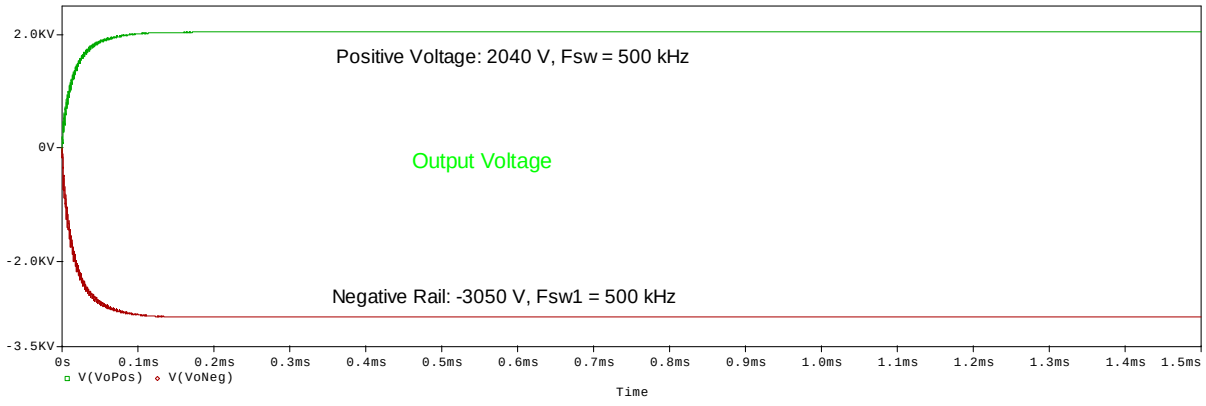

Figure 4.4: Output voltage results demonstrating maximum conversion requirements.

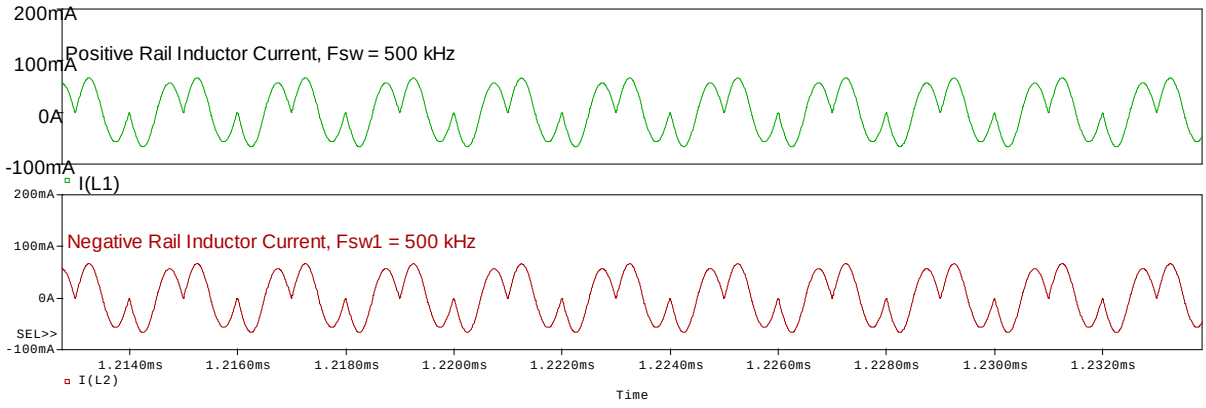

Figure 4.5: Both rails operating at BCM.

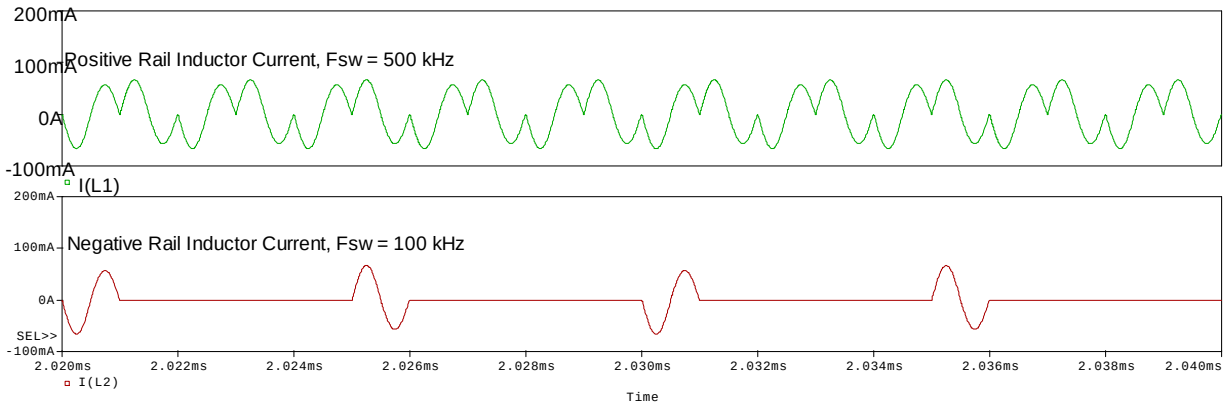

Figure 4.6: Positive rail remaining at BCM at 500kHz, Negative rail operating in DCM at 100kHz.

4.3 Negative Rail Optimization

In order to optimize the variability of the negative rail, it is necessary to investigate the relationship between changing switching frequency and the number of stages of voltage multipliers. While decreasing the switching frequency allows the negative rail to meet the -1000V condition, it requires too low a frequency to implement with a commercial off-the-shelf component. Further simulations were completed to determine the impact of varying numbers of voltage multiplying stages. The results can be seen below in Figure 4.7.

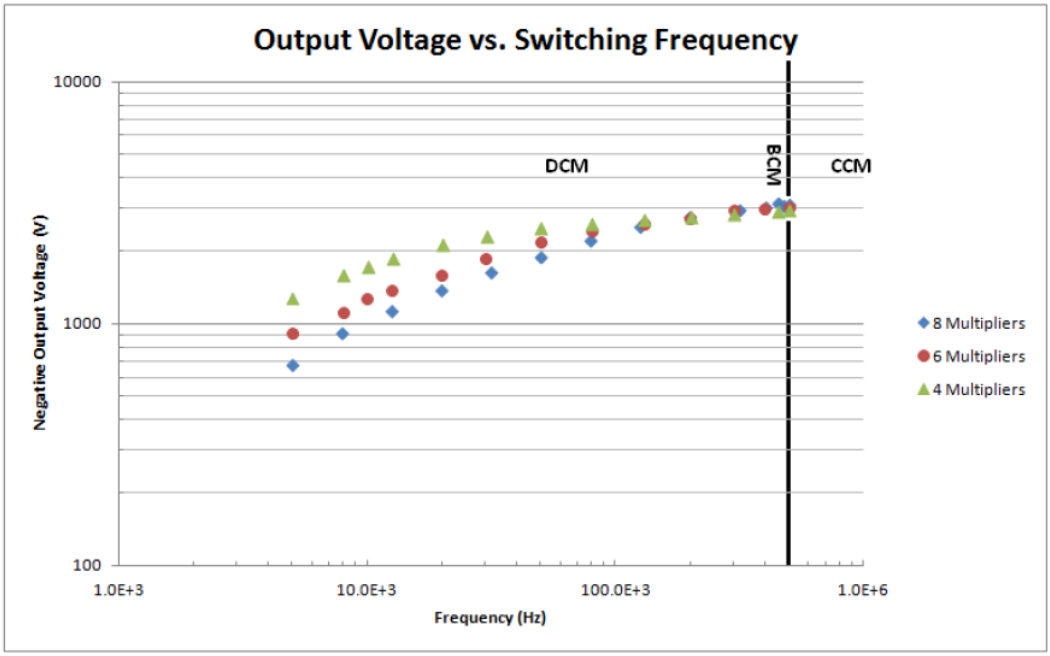

Figure 4.7: Output Voltage vs. Switching Frequency plotted for several cases of varying stages of voltage multipliers.

The result shows that with a larger number of voltage multiplier stages, lower output voltage can be obtained without having to drop the switching frequency as far as with fewer stages. This demonstrates that for the sake of contingency, the hardware implementation should account for more multiplication stages than necessary.

4.4 Component Ratings

From the results of the above simulations and design, it was possible to determine the ratings of each component within the design. These ratings are shown below in Table 4.1.

Table 4.1: Summarized component ratings.

Component	Rating
Bridge Switches	28 V, 2.5 A
Freewheeling Diodes	28 V, 2.5 A
Resonant Capacitor	14 V
Resonant Inductor	89 mA
Multiplier Components	800 V, 100 mA

5. Hardware and Results

With the requirements and specific parameters for each component in this converter defined in Chapter 4, the transition from simulation and design to hardware was now possible. For the sake of simplicity, only commercial off-the-shelf components were selected based on the requirements shown in Table 4.1. In order to provide an optimal design, several components meeting these requirements were selected and chosen based on best overall performance parameters and size.

5.1 Switching Stage

Tables 5-1 and 5-2 list the considerations of MOSFETs and freewheeling diodes that met the minimum requirements defined in Table 4.1. Table 5.1 shows that due to the extremely low R_{dson} property of the SUD50N04-8M8P, its small area and high power dissipation capabilities, it is the best choice. Table 5.2 shows that while the PMLL4148L appears to be the best option in terms of size and forward voltage, it is important to note that it is manufactured in a glass package, thus making it likely sensitive to the launch environment. While the S1A-13-F is larger, it is able to handle large spikes (since it can tolerate 1.0 A) that may result in hardware implementation.

Table 5.1: MOSFETs considered for implementation based on meeting the requirements shown in Table 4.1.

Part	Voltage Tolerance	Current Capability	Power Dissipation	Rdson(Ω)	Area (mm^2)
IRFR1N60ATRPBF	600 V	1.4 A	36 W	7	69.992
FDD3N40TM	400 V	2.0 A	30 W	3.4	41.8606
SUD50N04-8M8P	40 V	14 A	48.1 W	0.01	41.8606

Table 5.2: Freewheeling diodes considered for implementation based on meeting the requirements shown in Table 4.1.

Part	Voltage Tolerance	Current Capability	Forward Voltage (V)	Area (mm^2)
MMBD914-7-F	75 V	200 mA	1.25	7.5
S1A-13-F	50 V	1.0 A	1.1	13.432
PMLL4148L	75 V	200 mA	1	5.28

5.2 Resonant Stage

Table 5.3 lists the considered resonant stage capacitors. Because the output voltage is dependent on the ratio of switching frequency to resonant frequency, it is crucial that the resonant capacitor is constrained to a tight tolerance, especially under conditions of thermal fluctuation. For this reason, the VJ0805A102GXACW1BC is the best choice, despite its larger size.

Table 5.3: Resonant capacitors considered for implementation based on meeting the requirements shown in Table 4.1.

Part	Voltage Tolerance	Tolerance	Temperature Coefficient	Area (mm^2)
C1608C0G1H102J080AA	50 V	±5%	C0G, NP0	1.28
C1005X7R1H102K050BA	50 V	±10%	X7R	0.5
VJ0805A102GXACW1BC	50 V	±2%	C0G, NP0	2.5

5.2.1 Resonant Inductor/Transformer

Because of optimal size and meeting the necessary power and inductance requirements, CoilCraft's LPR6235 miniature step-up flyback transformers were selected. Several were sampled, varying between primary inductances of 7.5-25 µH, with ratios ranging from 1:20 to 1:100. Having several values allows for tuning based on different switching frequencies.

5.3 Voltage Multiplier

Table 5.4 lists the considered diodes for the voltage multiplication circuitry. Because the S1M-13-F is able to handle a higher voltage tolerance with the same total area, along with a lower amount of junction capacitance, it is the superior choice to the S1M-E3/61T and S1K.

Table 5.4: Voltage multiplication diodes considered for implementation based on meeting the requirements shown in Table 4.1

Part	Voltage Tolerance (V)	Current Capability (A)	Forward Voltage (V)	Area (mm^2)	Capacitance (pF)
S1M-13-F	1000	1	1.1	13.432	10
S1M-E3/61T	1000	1	1.1	13.432	12
S1K	800	1	1.1	13.432	12

Table 5.5 lists the considered capacitors for the voltage multiplication circuitry. Similar to the resonant capacitor, the VJ1210A102JXGAT5Z is the superior choice for its tighter tolerance and better temperature coefficient.

Table 5.5: Voltage multiplication capacitors considered for implementation based on meeting the requirements shown in Table 4.1

Part	Voltage Tolerance	Tolerance	Temperature Coefficient
C3216X7S3A102K085AA	1000 V	±10%	X7S
VJ1210A102JXGAT5Z	1000 V	±5%	C0G, NP0
CGA7K1X7R3D102K130KE	2000 V	±10%	X7R

5.4 Regulator

Due to the nature of SLR, a constant-on controller is the preferred choice. Initially, this was all that was investigated. Under further investigation, it was realized that the controllers chosen simply weren't able to provide the necessary switching signals (an example of the necessary switching signals is shown in Figure 5.1, with the recommended application schematic shown in Figure 5.2), even with the addition of

bridge drivers. For this reason, push-pull controllers were investigated, as the push-pull topology requires similar switching signals. Texas Instruments manufactures a chip, the LM5037 that could serve this purpose, with the exception that it requires 12 V to power it. In an effort to avoid an extra power regulator to power the chip alone, the LM25037 was been chosen, as it is equivalent in most regards, the main exception being that it can operate at 5.5 V. An initial simulation was run based on this chip and the previously simulated ideal models. During this simulation, the required maximum output voltages were obtained as shown in Figure 5.3 below.

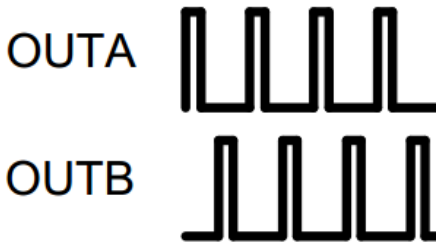

Figure 5.1: Example of the necessary switching signals.

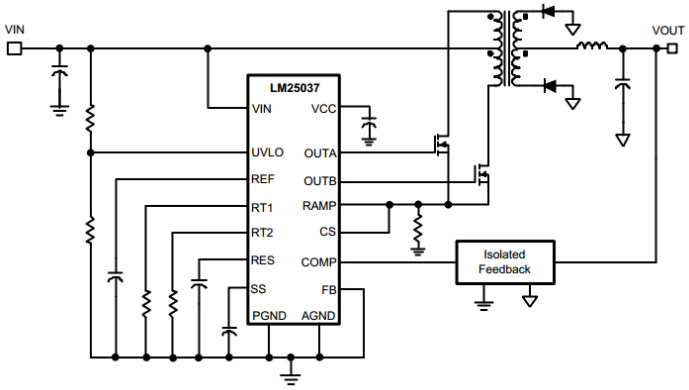

Figure 5.2: Schematic of the LM25037 implemented as a push-pull topology with supporting circuitry [18].

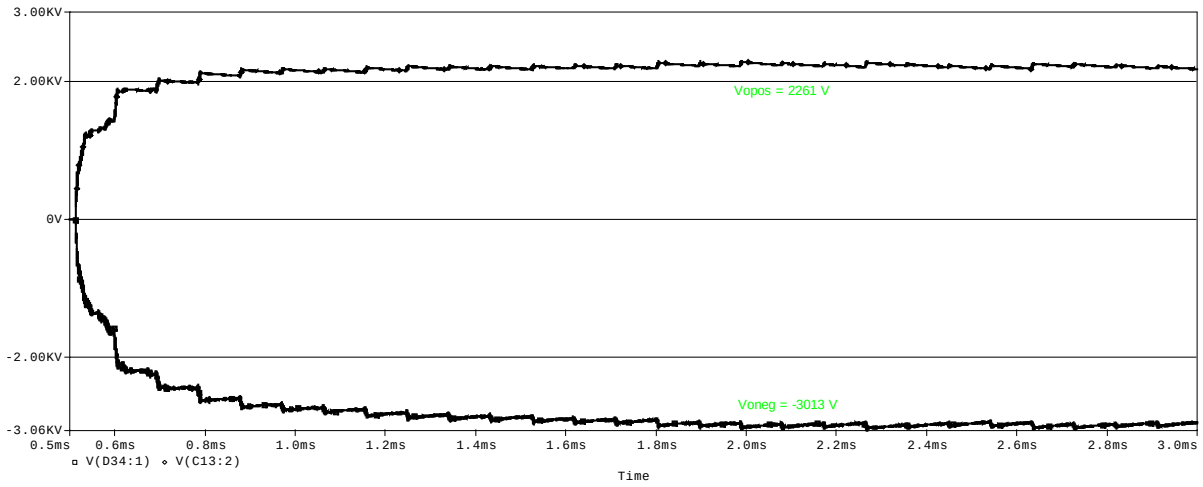

Figure 5.3: Results of basic simulation in OrCAD.

5.5 PCB Layout and Implemented Schematic

Figures 5.4 through 5.7 detail the schematic used to create the netlist for the board layout shown in Figures 5.8 and 5.9. In order for a layout to be accommodated within a CubeSat, the board must not require more than 100 cm^2. In order to allow for easy debugging, component arrangement was intentionally made sparse. The implemented circuit board (shown in Figures 5-8 and 5-9) is 104 cm^2, just over the limit allowed within a CubeSat. As mentioned, this also allowed for ample debugging room, and the board can be shrunk well within the required 100 cm^2. The top layer contains the majority of the circuitry, whereas the bottom layer contains grounding planes as well as the voltage multiplication circuitry. The section labeled “CONTROLLER” contains the footprint for the LM25037 and the appropriate supporting circuitry, including the switching frequency tuning resistors RT1 and RT2, as seen in Figure 5.4. The “SIGNAL INVERSION” section contains the circuitry shown in Figure 5.5, which is meant to provide signal inversion so as to drive the PMOS switches on the high side of the bridge.

The “BRIDGE” and “RESONANT LOAD” sections are both shown in Figure 5.6, and include extra 0Ω resistors for debugging and probing purposes, as well as the series resistance R9 for current sensing capability. The output stage of voltage multiplication and classic rectification are included in Figure 5.7, labeled as “VOLTAGE MULTIPLICATION” and “RECTIFIER LOAD” in Figures 5.8 and 5.9. The rectifier load was added in for contingency in the event that the voltage multiplication section was non-functional. For further contingency, 16 voltage multiplication stages were allotted for as opposed to the 8 shown to be necessary in Figure 4.7. Just in case any items were forgotten, the “DEBUG/WIREMOD PADS” provide extra room to act as a breadboard type work area.

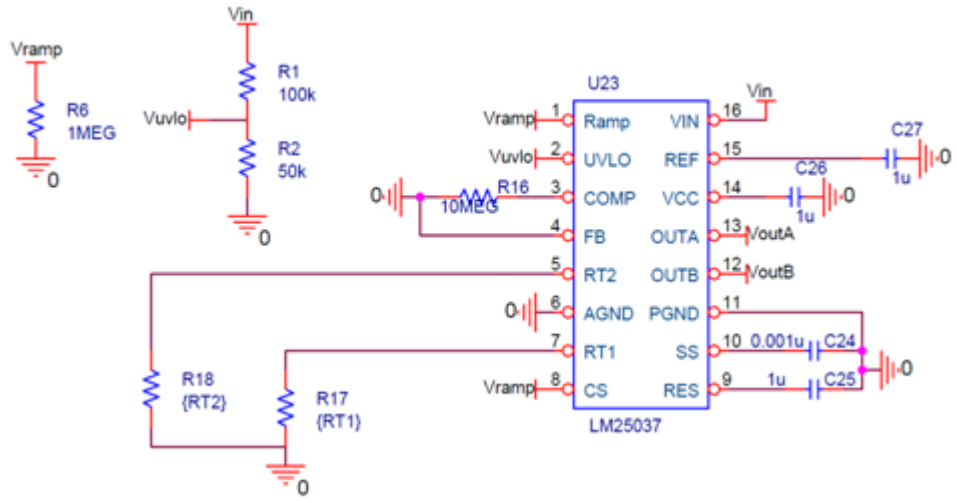

Figure 5.4: Controller and supporting circuitry.

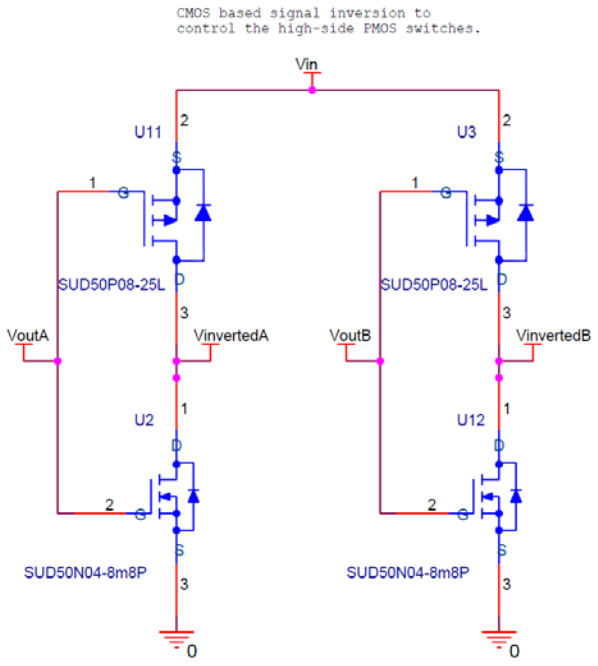

Figure 5.5: Signal inversion circuitry for driving the high-side of the full bridge.

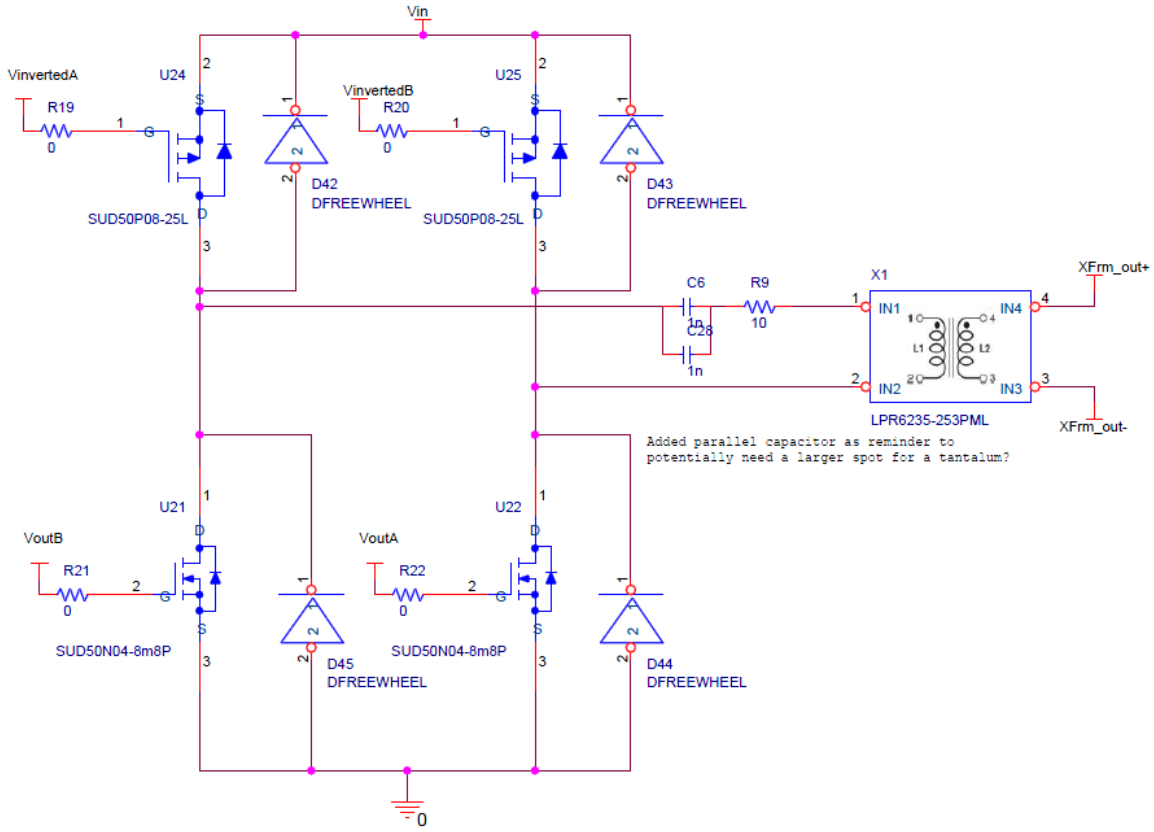

Figure 5.6: Full bridge implementation and resonant load sections.

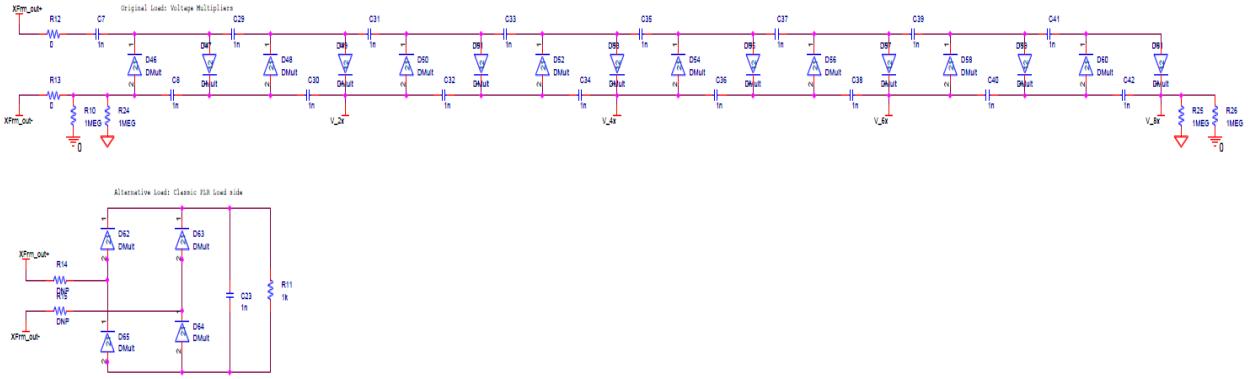

Figure 5.7: Voltage multiplication circuitry, including the standard rectification bridge for testing purposes.

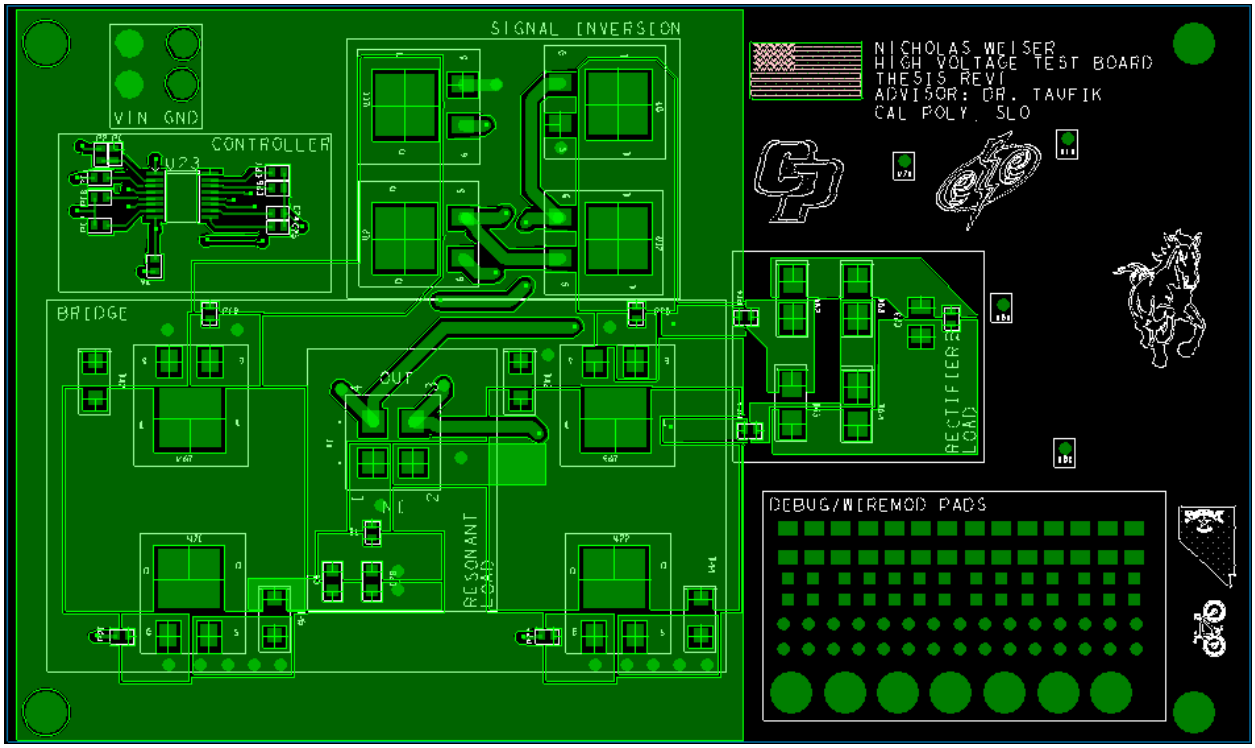

Figure 5.8: Top layer of the designed PCB.

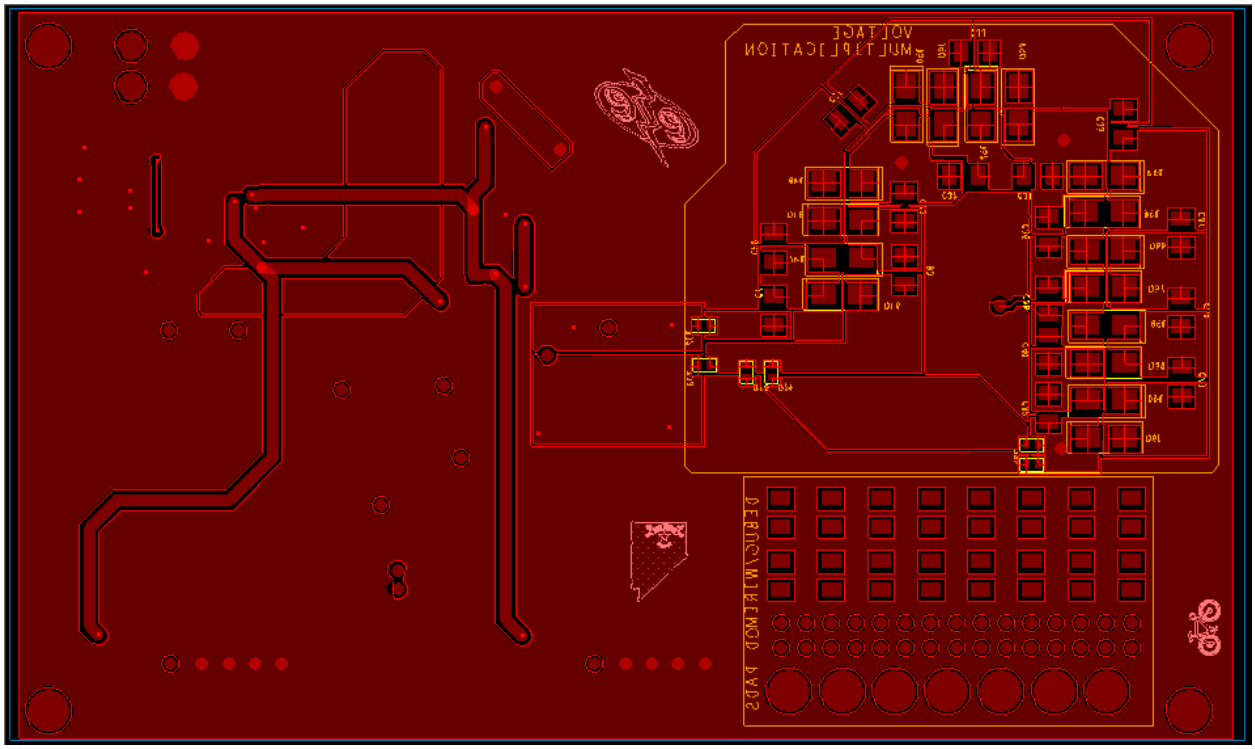

Figure 5.9: Bottom layer of the designed PCB.

5.6 Hardware Results

5.6.1 Revision 1

The first build consisted of only the controller and signal inversion sections of the board. The test setup for this is shown in Figure 5.10. During testing, it was discovered that the components chosen for the signal inversion section, while simple in implementation, were not meant for this purpose. Specifically, the CMOS inversion scheme shown in Figure 5.5 implemented MOSFETs that were not matched, which resulted in both switches conducting simultaneously. However, it was shown that the nominal switching scheme was functional, as seen in Figure 5.11. The results of adding the inversion circuitry is shown in Figure 5.12. The yellow signal should be a simple square wave, as seen in Figure 5.11, and the blue signal should be the inverse of the yellow. Not only did

the inversion scheme introduce a shorting situation, but substantial noise was added. Further investigation also showed that the MOSFETs inherently contain to large of a gate capacitance to handle the 500 kHz signal shown in 5.11. An attempt was made to simply run the system at a lower switching frequency (25 kHz), but this still resulted in partial overlap of conduction between the PMOS and NMOS switches as seen in Figure 5.14. The input signal is shown in blue, and the output shown below in purple. The NMOS signal clearly turns partially on in the attempt at a full square wave, but does not go into full conduction mode until the PMOS turns on, hence the double step shown. The test setup for this is shown in Figure 5.13. In order to combat these issues, the CMOS inversion scheme was replaced with an open-drain inverter (Figure 5.15), as well as running the system at lower switching frequency, specifically 40 kHz. While still slightly non-ideal and noisy, this resulted in a workable gate driving signal scheme, shown in Figure 5.16.

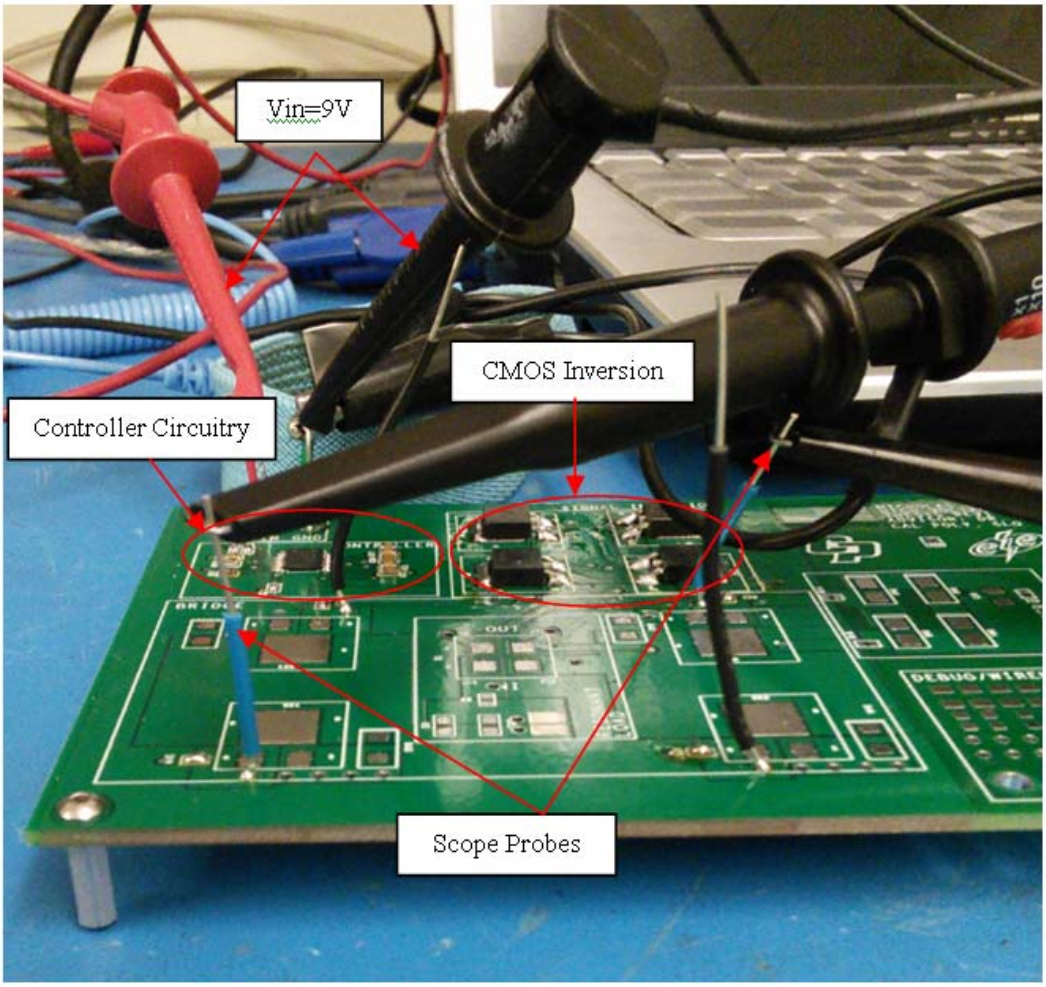

Figure 5.10: Test set up for revision 1, including controller and signal inversion circuitry.

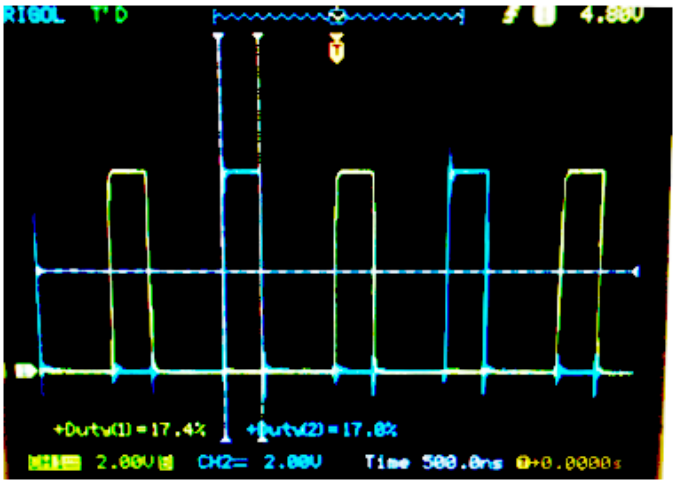

Figure 5.11: Push-Pull gate driving signals in revision 1 behaving nominally, before implementation of inversion circuitry.

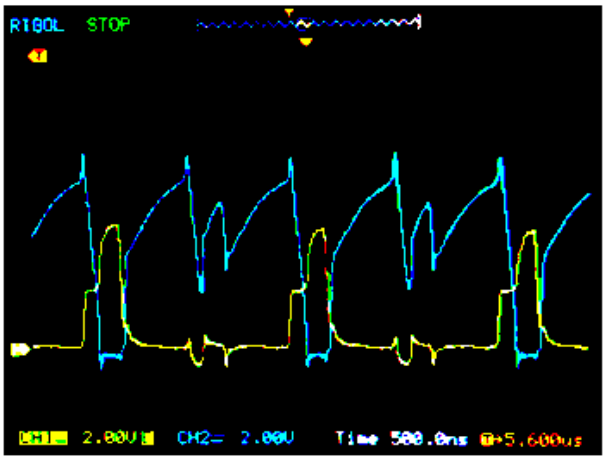

Figure 5.12: Resulting signals showing negative effects of mismatched MOSFETs implemented in the CMOS inversion scheme.

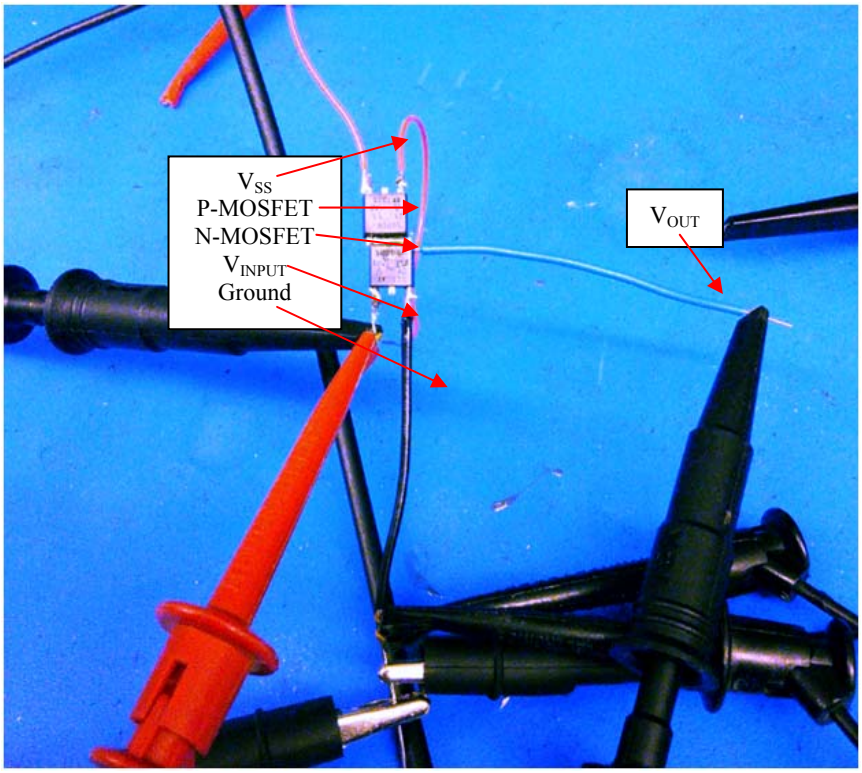

Figure 5.13: Test setup for CMOS inversion scheme.

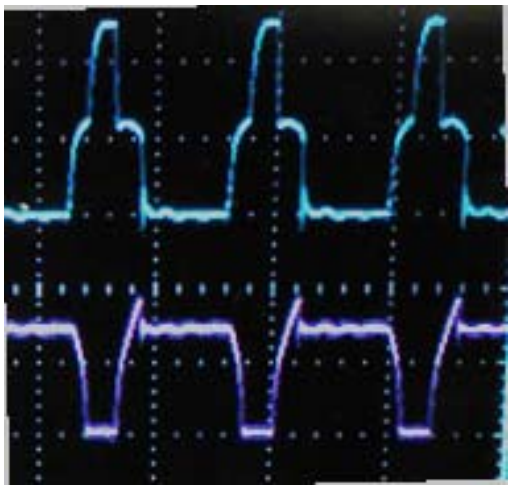

Figure 5.14: Operating the CMOS inversion scheme at a lower switching frequency (25 kHz) still resulted in both the PMOS and the NMOS switches turning on simultaneously.

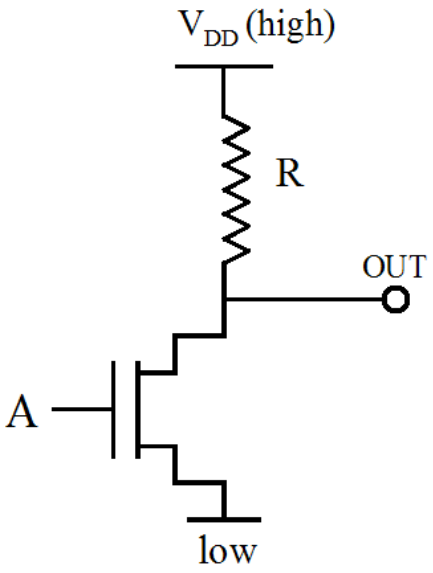

Figure 5.15: Open-Drain inversion scheme implemented to replace the CMOS inversion scheme [20].

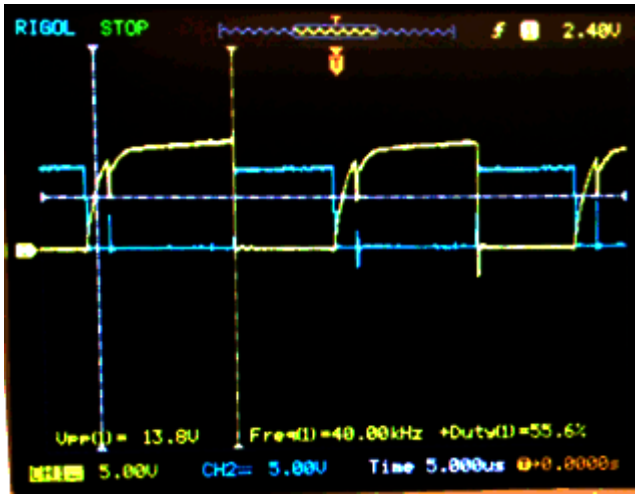

Figure 5.16: Results of implementing the open-drain inversion scheme.

Next, the bridge and resonant load circuits were added. This test setup is shown below in Figure 5.17. For the same reasons as described above, specifically that the MOSFETs used in this bridge configuration are not appropriately matched, there was too severe of an overlap in conduction modes, resulting in shorting during switching periods. This caused the bench top power supply to go into constant-current mode and output only 5 V as opposed to the set 9 V, which is below the recommended operating voltage of the LM25037. This caused the controller to create non-nominal switching signals, as seen in Figure 5.18. Despite these issues, the inductor current still operated roughly within discontinuous conduction mode, as shown by the red signal below. It was clear at this point that the hardware choices were no longer sufficient.

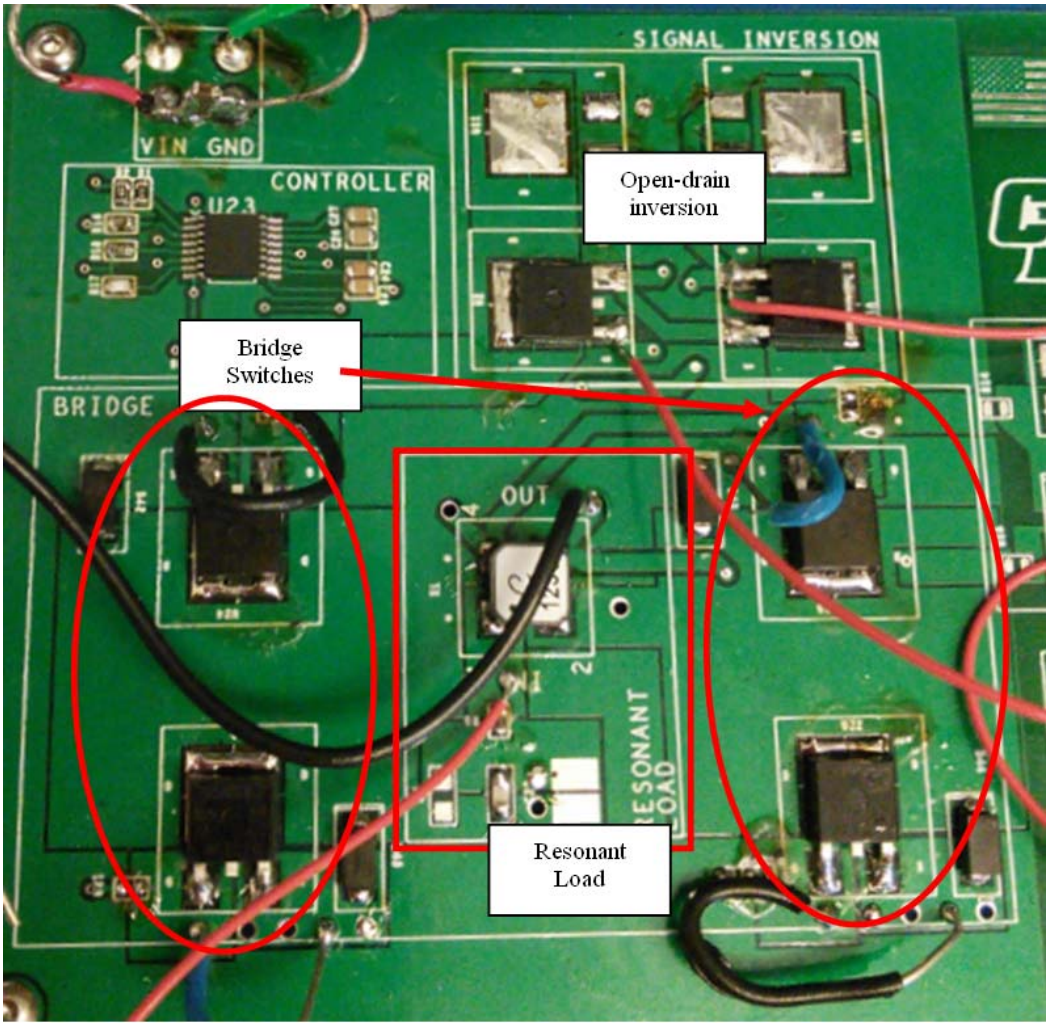

Figure 5.17: Similar to Figure 5-10, but now with the resonant load and bridge switches added.

Figure 5.18: Result of implementing the bridge and resonant load of Figure 5-6, showing non-nominal switching scheme and resultant discontinuous conduction mode current.

5.6.2 Revision 2

Because the issues discussed above are the result of mismatched bridge switches that turn on simultaneously, resulting in shorts during switching transitions, a proper bridge driver was implemented. The part chosen was the TA8428K(S), a Toshiba product that is meant for full bridge brush motor rotation control. The block diagram and recommended application schematic are shown in Figures 5.19 and 5.20. For the sake of easy signal manipulation, this bridge driver was interfaced with an Arduino Uno. The Arduino provided the switching signals to the IN1 and IN2 pins on the driver, and the output pins OUTA and /OUTA were connected to only the resonant load section of the circuit board shown in Figure 5.8. At this point, the circuit board was being used only for the resonant load and voltage multiplication, as seen in Figures 5.21 and
5-22. The voltage multiplier stages were connected such that 8 stages of multiplication could be obtained. In order to sense the output voltage at this point without damaging any equipment, the 8x multiplier was connected to a 1:31 voltage divider which was added to the debug pads in the bottom right corner of the circuit board. The first case tested was with a 50.8 kHz signal. The resonant load was the series combination of the LPR6235-123Q, a 1:50 turns ratio, 12.5 uH primary side inductance transformer, and a 100 nF capacitor. This produces a nominal resonant frequency of 142 kHz, so driving the gate signals at 50.8 kHz is well within the nominal operational range of DCM, which requires the ratio of the switching frequency to resonant frequency to be less than 0.5. The result of this test is shown in Figures 5.24 through 5.26.

Figure 5.24 demonstrates discontinuous conduction mode current behavior in red. The input to the resonant load, seen as OUT1 and OUT2 in Figure 5.21 is seen in the yellow

and blue signals. As a means of verifying the voltage multiplication scheme, the peak values of the transformer voltage were also measured, as seen in green in Figure 5.25. This peak value of 216 V would ideally be multiplied by 8 to 1.728 kV, but due to losses inherent in conduction paths and voltage drops across the diodes, as well as ESR in the capacitors, the peak value is instead

31*53.5 = 1.659 kV, which is only 4% lower than the 1.728 kV ideal value. Figure 5.26 shows a zoomed in view of the inductor current, which can be seen to more closely follow the simulated waveforms shown in Figure 4.6.

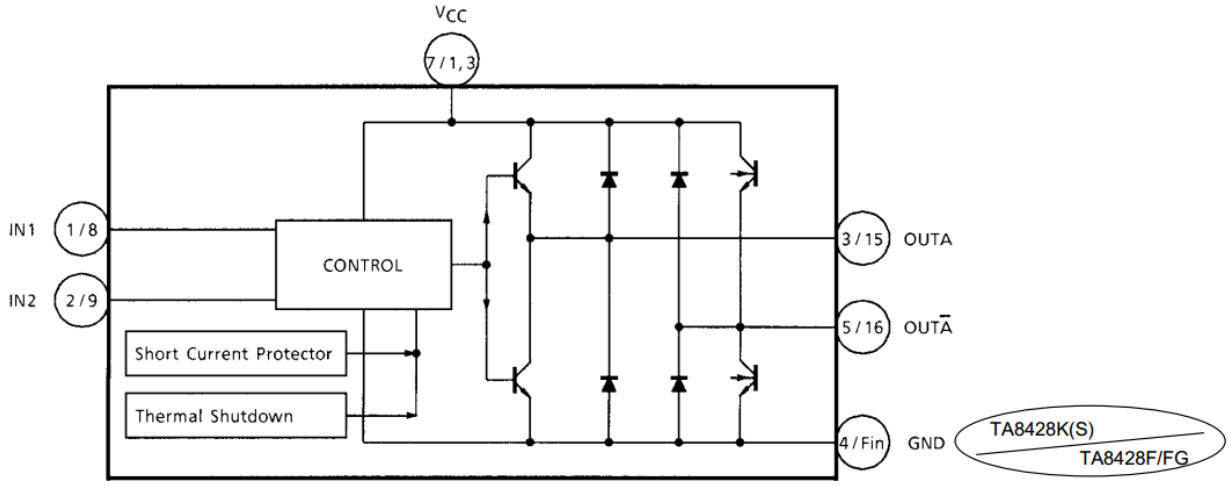

Figure 5.19: Block diagram for the TA8428K(S) [21].

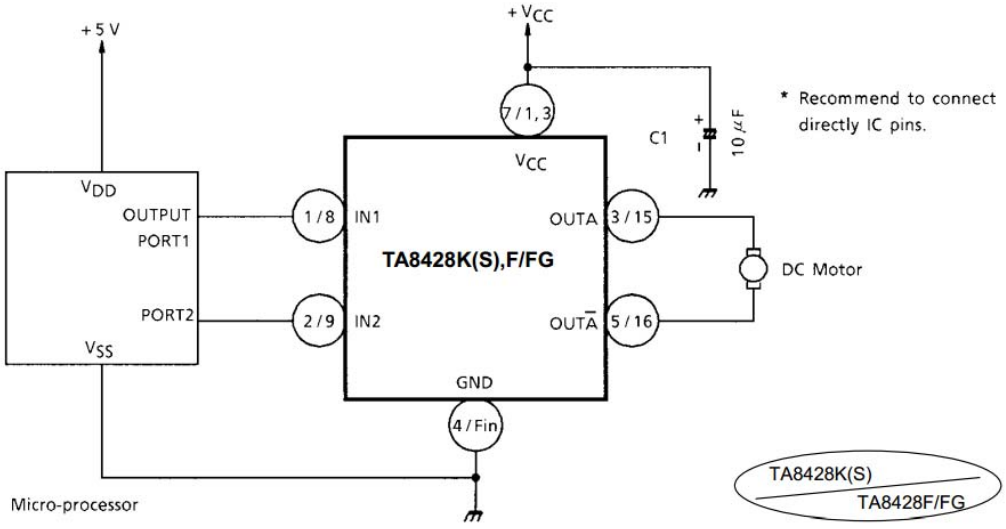

Figure 5.20: Recommended application schematic [21].

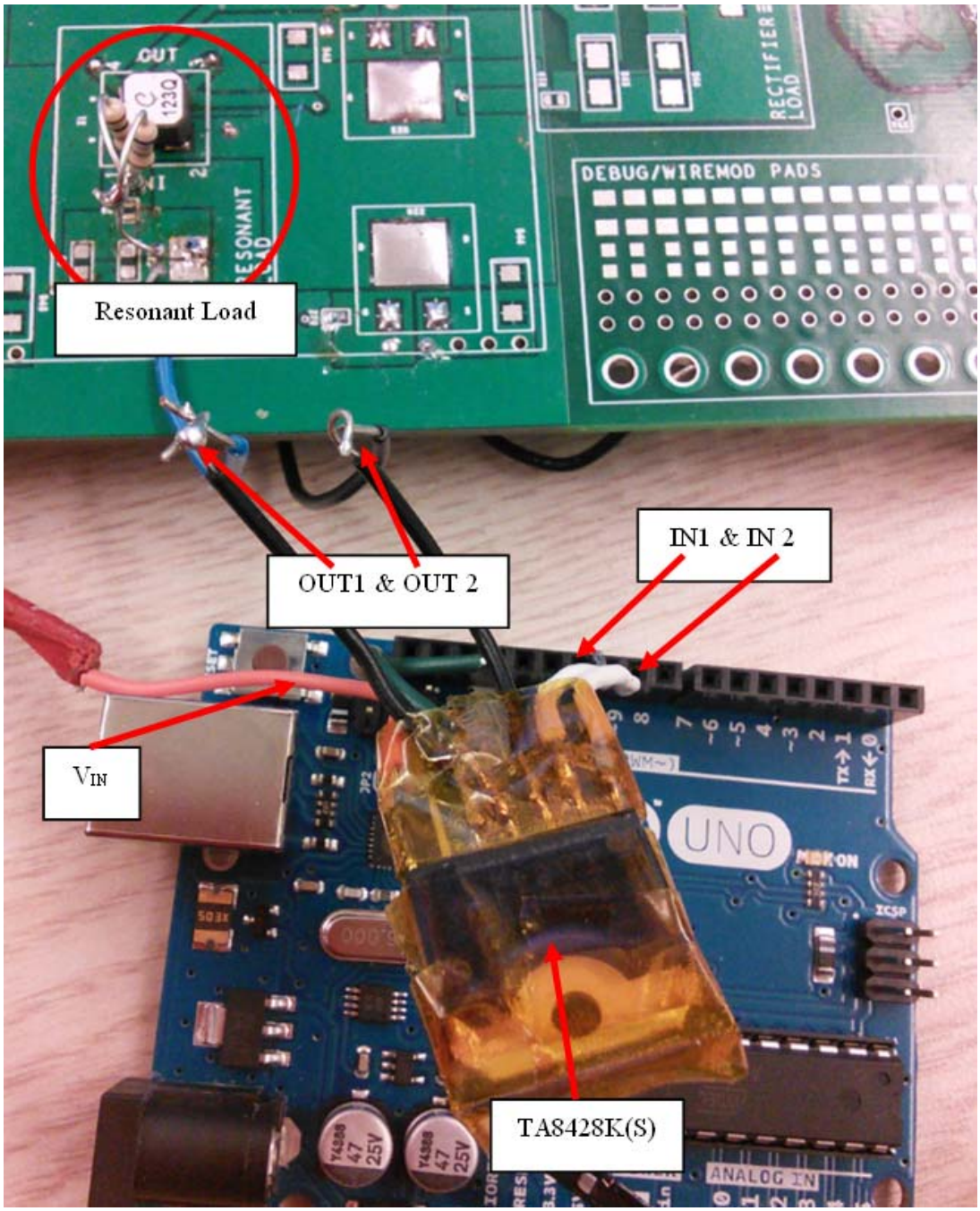

Figure 5.21: Replacement components for the controller and bridge components.

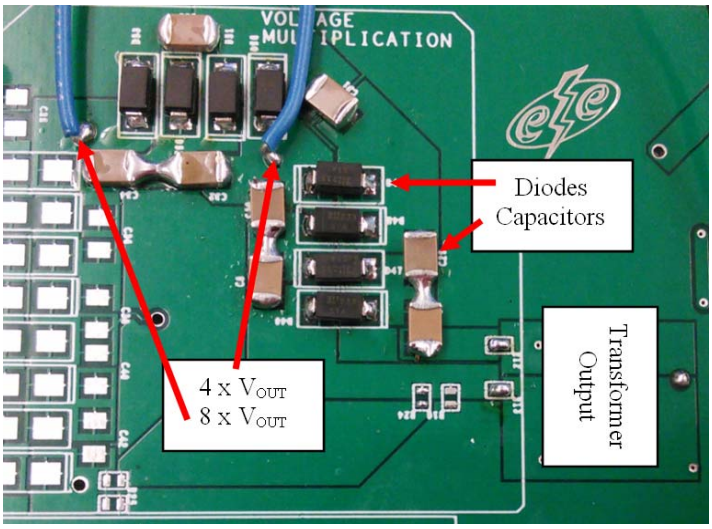

Figure 5.22: Voltage multiplication stage.

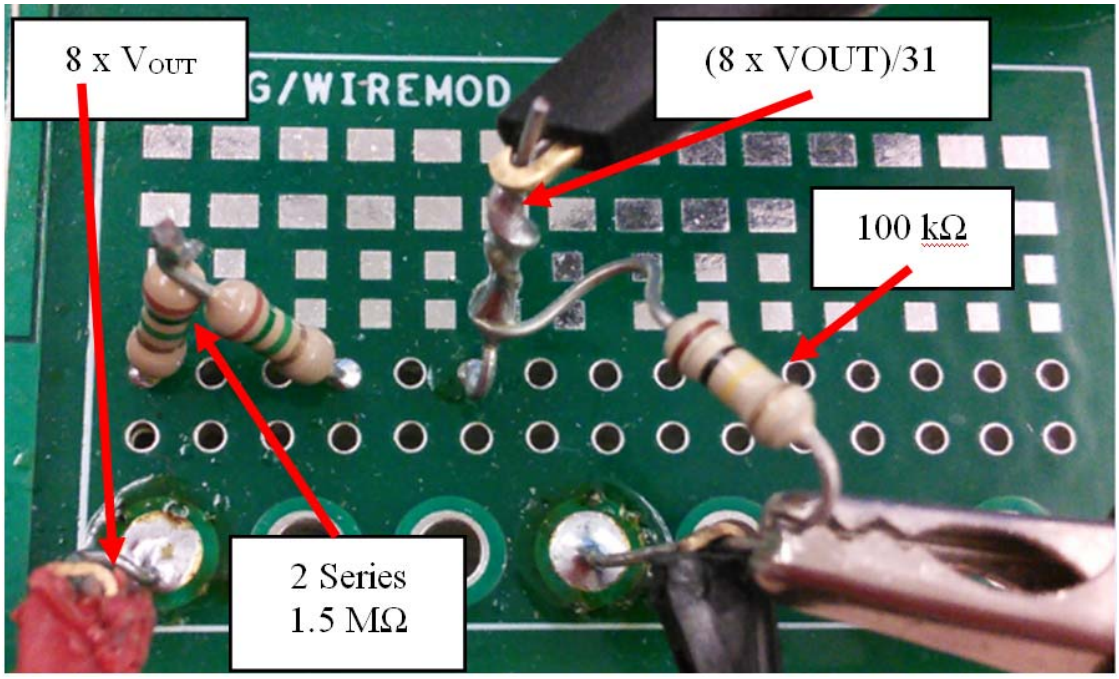

Figure 5.23: The implemented 1:31 voltage divider for output voltage sensing.

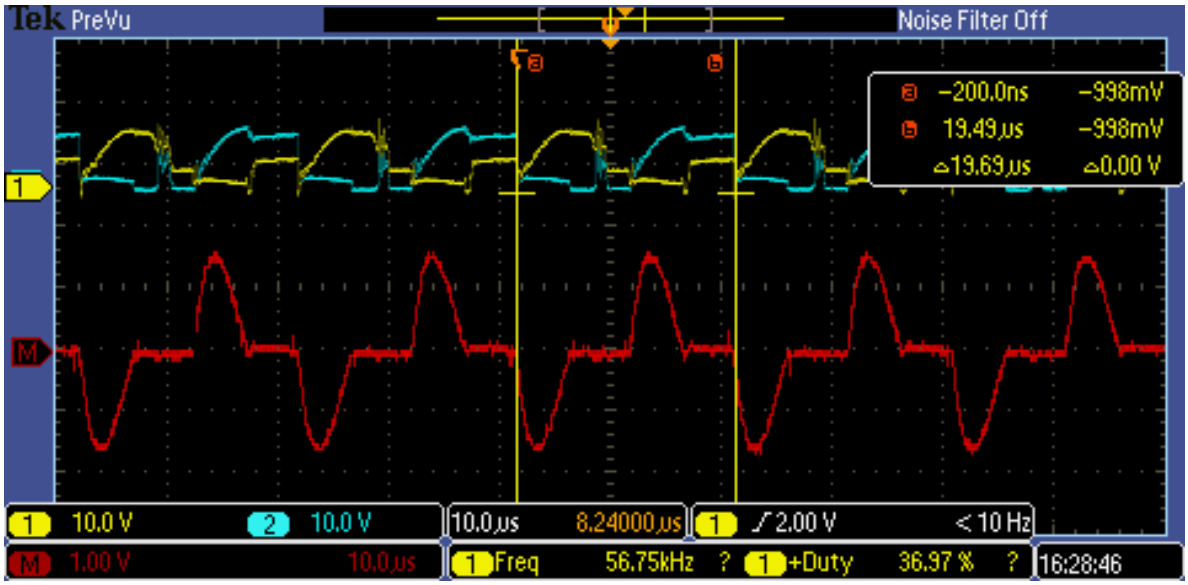

Figure 5.24: Result of the Arduino and bridge driver system, showing inductor current.

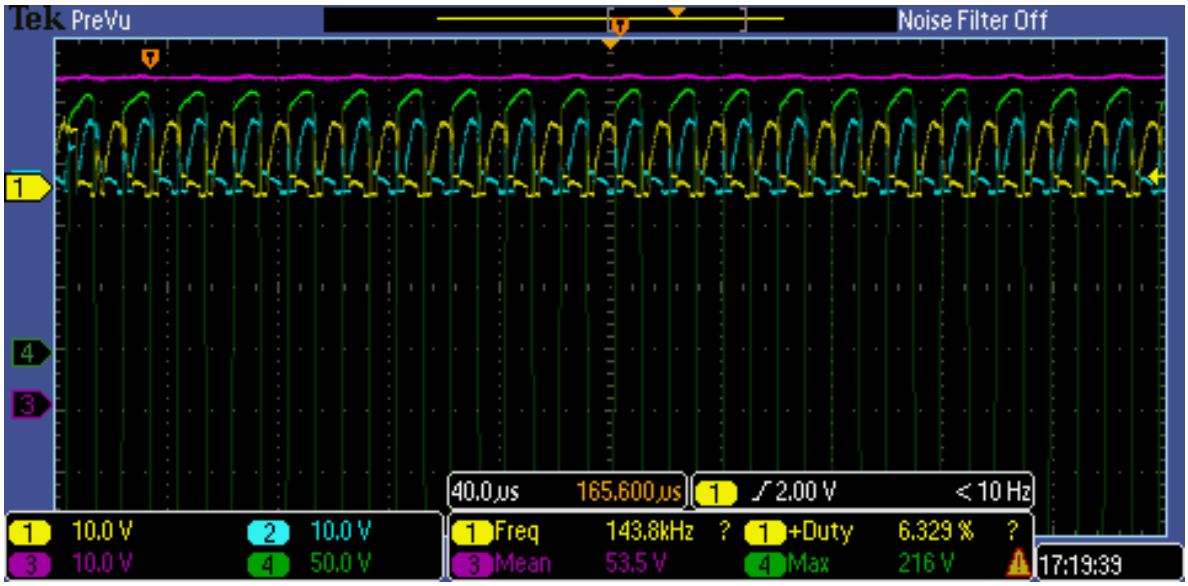

Figure 5.25: Result of the Arduino and bridge driver system, showing output voltages.

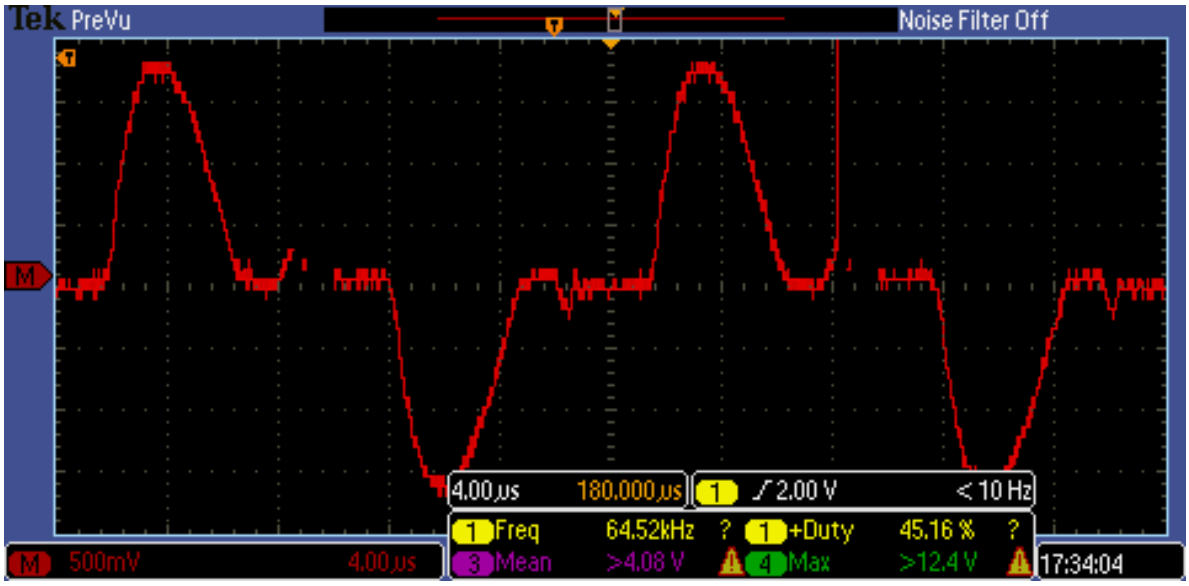

Figure 5.26: Zoomed in view of the resonant inductor current, roughly matching the signal shapes shown in Figure 4-16.

This system performs much closer to the simulated results seen in Chapter 4. As seen in Figure 4.7, at this frequency the expected output voltage is 1897 V, and the result in Figure 5.25 demonstrates this system operating very closely to this at the 50.8 kHz frequency, outputting 53.5 V * 31 = 1658 V. While small losses were accounted for in the simulation resulting in Figure 4.7, the conduction losses and noise present in the switching signals, as seen in

Figure 5.24, result in non-idealities, causing this loss. There is also loss inherent in the diodes in the voltage multiplication section which causes further voltage drop. The 8 stages of voltage multiplication also only multiply by 7.7, another problem caused by conduction losses and voltage drops across the diodes.

Next, the switching frequency was varied to demonstrate variable output capabilities, the results of which are shown in the graph in Figure 5.27. The implemented system is shown

to be less smooth than the simulated results in Figure 4.7. This is caused by different Q values of the capacitors and the inductor, which results in different drops and losses based on the filtering effects of these components. Also, use of the system results in thermal losses, placing some of the components, specifically the inductor, into different conduction modes resulting in varied values.

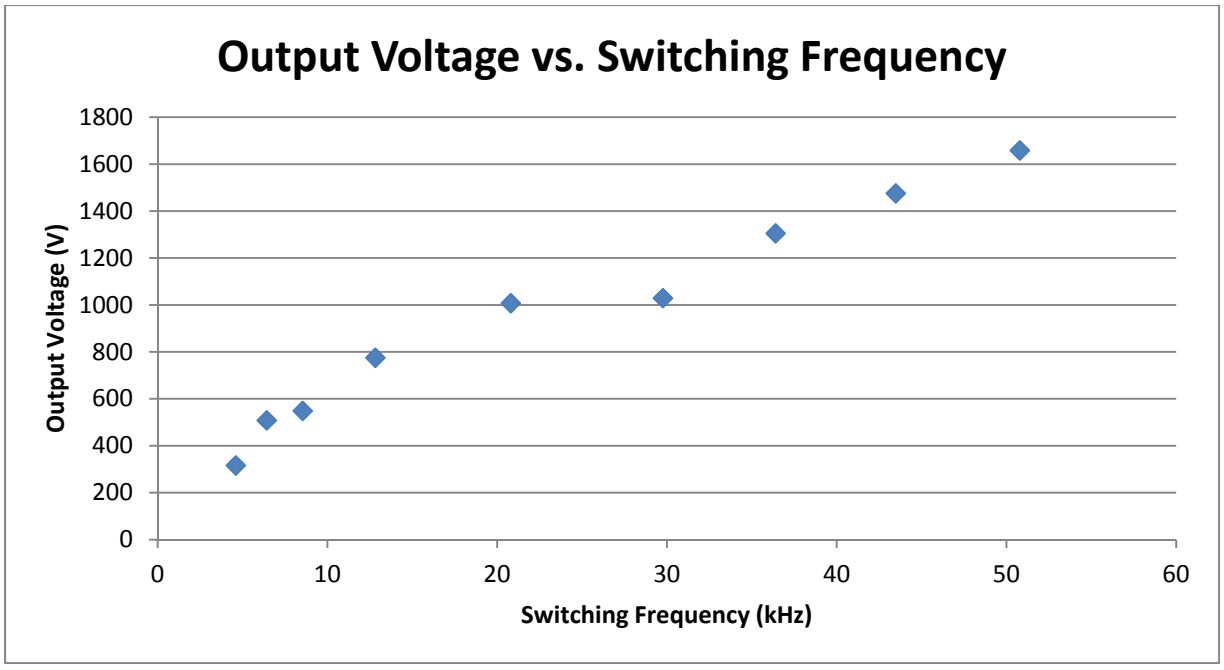

Figure 5.27: Output voltage vs. switching frequency.

In order to verify both the ripple requirement as well as the negative voltage capability, the 1:31 divided signal was applied to an AC coupled scope probe, and cursors were used to measure the worst case ripple. This was observed to occur at 50 kHz, and results in a 1.06 V ripple at the maximum output voltage. Since the AC signal is also stepped down by the 1:31 divider, taking this ripple voltage and dividing it by the DC signal shown in purple gives a ratio of

1.96/59.9 = 0.03, resulting in a 3.2% ripple, thus meeting the <5% requirement, as seen in

Figure 5.28. The results of operating the negative converter can be seen in Figures 5.28 and 5.29, which shows that -55.2*31 = -1.71 kV can be obtained by this converter.

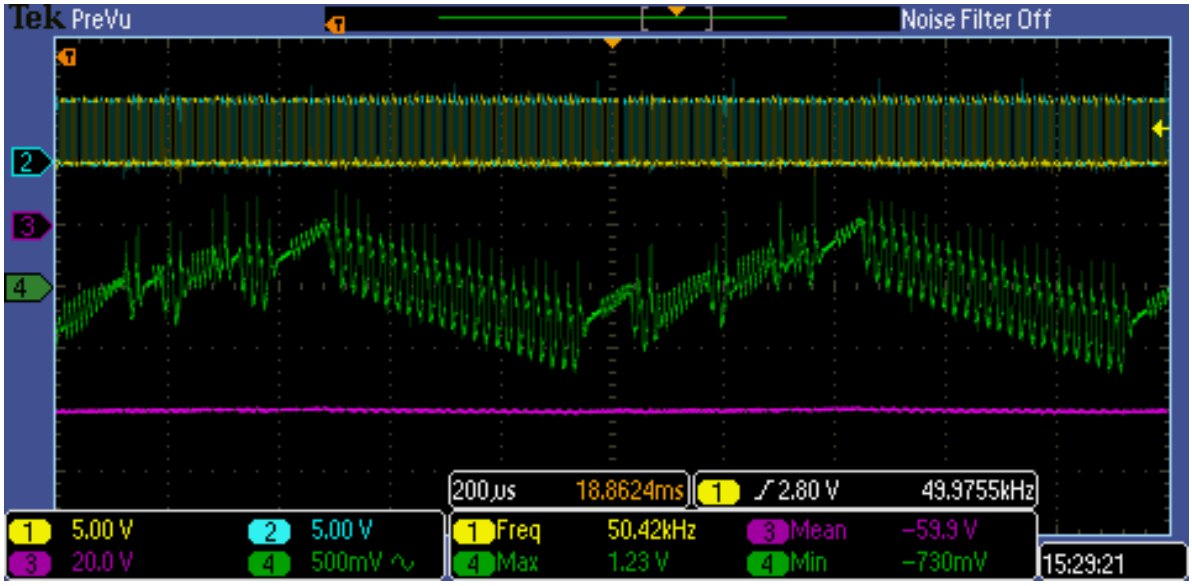

Figure 5.28: Worst case ripple measurement

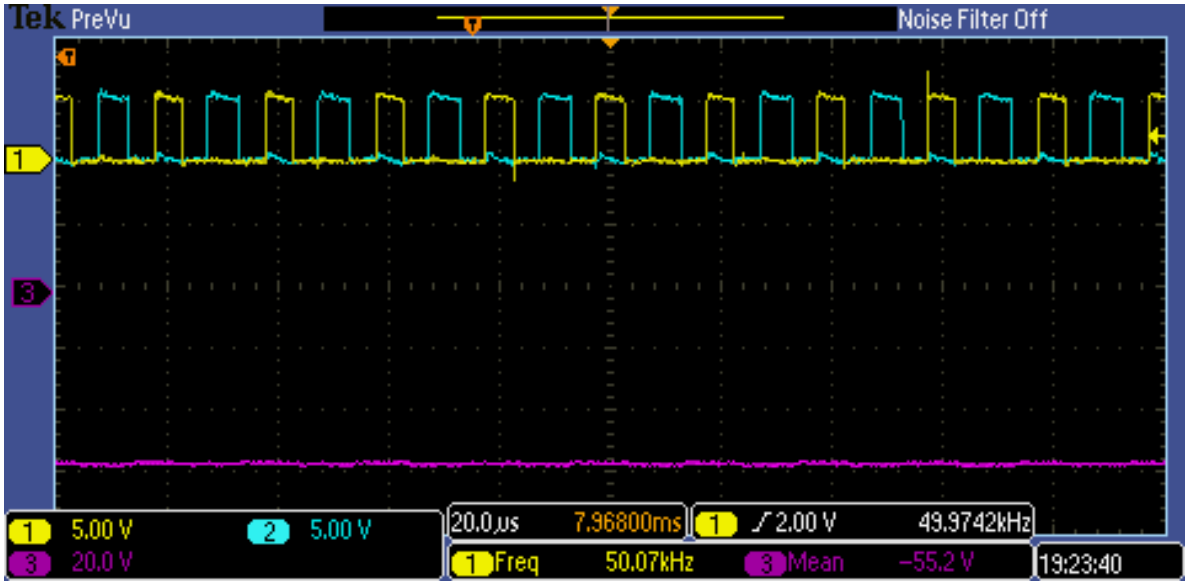

Figure 5.29: Negative output voltage functioning properly.

5.7 Summary of Results

Table 5.6: Primary Requirements definitions set by NASA-JPL with results and comments.

Primary Requirement	Condition	Results	Comments
P.S. #1 Output Voltage	2000 V (constant)	1658 V	Proof of Concept
P.S. #1 Output Current	> 1.8 mA	0.534 mA	
P.S. #2 Output Voltage	-1000 ↔ -3000 V	396 V ↔ 1658 V	Measured on the Positive rail for demonstration purposes
P.S. #2 Output Current	> 0.1 mA	0.552 mA	Exceeded Requirement
Output voltage ripple	< 5% ripple	3.2%	

Table 5.7: Secondary Requirements definitions set by NASA-JPL with results and comments.

Secondary Requirement	Condition	Results	Comments
Overall system mass	50 grams maximum	82 grams	Proof of Concept
Overall system volume	0.25 U maximum (2.5 cm x 10 cm x 10 cm)	0.15 U	Can be further minimized
EMI	Low	DCM operation	Can be further tested

Tables 5.6 and 5.7 tabulate the accomplishments of this converter. Due to the necessity of operating the system at a much lower switching frequency than designed, the resulting output voltage and current was also lower. Also, for this draft implementation, the overall system mass was 32 grams over the required maximum, which can be further minimized by removing the debugging pads, as well as other unused board space. Both rails were able to operate within the 5% ripple requirement, while simultaneously operating within DCM, providing low EMI outputs. Finally, the system was able to be maintained within the overall volume requirement thanks to the use of low profile components, specifically the CoilCraft transformer. This can of course be further minimized by reducing the board space as mentioned above.

6. Conclusion

This thesis project proposed the design and implementation of a DC-DC high voltage power supply for use on board a CubeSat class spacecraft. This power supply took the specific requirements of the spacecraft into consideration during the design and implementation, including parameters such as mass, volume, and low EMI. The overall mass of the system is slightly above the requirement, but this can be fixed with a secondary board revision that does not include the Arduino or debugging ports. The Arduino was implemented only for the sake of generating the switching signals to the bridge. The volume of the system was maintained within the limits provided, which can be attributed to the use of low profile components, including the CoilCraft transformer. Operation in a lowered EMI state was achieved by implementing discontinuous conduction mode. In the future, it would be useful to record specific values of measured EMI to fully prove the converter's capabilities. The converter was designed to accept power from Lithium-Ion battery and solar panel sources and generate a maximum of 5 kV for the purpose of providing power to ion-spray propulsion thrusters. While the implemented circuit board uses only operates one rail at a time, it is a sufficient proof of concept, as it can be modified to produce negative voltages as well. The implemented converter did not meet the maximum voltages due to lowered switching frequency operation as well as non-ideal components, but this can be ameliorated by adding further stages of multipliers to achieve the

+2 kV and -3 kV requirements. Another improvement to the system would be to find a smaller, lower power system (as compared to the Arduino) to generate the gate driving signals, since the LM25037 proved to be an unstable controller. The Arduino is both

overcomplicated for the task, as well as unnecessarily large and power hungry, as well as more expensive ($30 compared to potentially less than $10). It served to prove the concept of using this topology to generate high voltage signals, but using standalone square wave generators would be a better option. Because the implemented converter ran at a maximum of 50 kHz, a 555 timer type system could be implemented, as an example. There is also a fair amount of noise still inherent in the switching signals, as seen in Figure 5.24, which is due to poor signal routing on the PCB, as well as added inductance from the wire modifications used to interface the Arduino to the TA8428K(S), as well as interfacing the TA8428K(S) to the resonant load. Finally, it would be worthwhile to test the system in a thermal-vacuum chamber, which would prove the capabilities of the converter to operate in near-space conditions.

In conclusion, this thesis has demonstrated the capability of the series loaded-resonant topology to be implemented as a high voltage DC-DC converter for use on board a CubeSat class spacecraft.

Works Cited

[1] CubeSat, "CubeSat Design Specification Rev. 12," 1 August 2009. [Online]. Available: http://cubesat.org/images/developers/cds_rev12.pdf. [Accessed 1 January 2014].

[2] CubeSat, "PPOD MK-II Renderings," 09 November 2009. [Online]. Available: http://cubesat.org/index.php/media/pictures/55-p-pod-mk-ii-renderings. [Accessed 18 February 2014].

[3] L. Friedman, "Testing Sail Deployment," Planetary Societ, 06 03 2011. [Online]. Available: http://www.planetary.org/blogs/guest-blogs/lou-friedman/20110306.html. [Accessed 8 5 2014].

[4] NRL, "NRL's TEPCE Spacecraft Undergoes Successful Deployment Test - See more at: http://www.nrl.navy.mil/media/news-releases/2010/nrls-tepce-spacecraft-undergoes-successful-deployment-test#sthash.GyoMBzak.dpuf," 19 5 2010. [Online]. Available: NRL's TEPCE Spacecraft Undergoes Successful Deployment Test - See more at: http://www.nrl.navy.mil/media/news-releases/2010/nrls-tepce-spacecraft-undergoes-successful-deployment-test#sthash.GyoMBzak.dpuf. [Accessed 9 5 2014].

[5] Tethers Unlimited, "CubeSat Terminator Tape," [Online]. Available: http://www.tethers.com/SpecSheets/Brochure_TermTape.pdf. [Accessed 9 5 2014].

[6] C. Healy, "TetherSat 1,2," 2009. [Online]. Available: http://ccar.colorado.edu/asen5050/projects/projects_2009/healy/. [Accessed 10 5 2014].

[7] NASA, "Blue Solar Sail," 18 6 2008. [Online]. Available: http://www.nasa.gov/mission_pages/smallsats/nsd_bluesail.html. [Accessed 2014 8 5].

[8] J. Mueller, R. Hofer and J. Ziemer, "Survey of Propulsion Technologies Applicable to CubeSats," Jet Propulsion Laboratory, National Aeronautics and Space Administration, Pasadena, CA, 2010.

[9] D. Parker, "1.5m Telescope With Laser, Starfire Optical Range," 8 May 2013. [Online]. Available: http://fineartamerica.com/featured/1-15m-telescope-with-laser-starfire-optical-range-david-parker.html.

[10] AustinSat, "Thruster Spec Sheet R5," 2013. [Online]. Available: http://austinsat.net/wp-content/uploads/2013/07/Thruster-Spec-Sheet-rev5.pdf. [Accessed 5 5 2014].

[11] C. Loef, "Power Supply for an X-Ray Generator," 23 5 2006. [Online]. Available: http://pdfpiw.uspto.gov/.piw?Docid=07050539&homeurl=http%3A%2F%2Fpatft.uspto.gov%2Fnetacgi%2Fnph-Parser%3FSect2%3DPTO1%2526Sect2%3DHITOFF%2526p%3D1%2526u%3D%25252Fnetahtml%25252FPTO%25252Fsearch-bool.html%2526r%3D1%2526f%3DG%2526l%3D50%2526d%3DPALL%2526S1. [Accessed 14 3 2014].

[12] J. Martin-Ramos, "Power Supply for a High-Voltage Application," *IEEE,* vol. 23, no. 4, pp. 1608-1619, 2008.

[13] I. Krichtafovitch, "MODULAR HIGH-VOLTAGE POWER SUPPLIES

DESIGN," *IECEC,* vol. 1, pp. 375-380, 1996.

[14] C. Ccapellati, "High Voltage Power Supplies for Analytical Instrumentation".

[15] Clyde-Space, "University of Glasgow and Clyde Space set to put brakes on space junk problem," 19 November 2012. [Online]. Available: http://www.clyde-space.com/news/355_university-of-glasgow-and-clyde-space-set-to-put-brakes-on-space-junk-problem. [Accessed 1 February 2014].

[16] J. Parker, "The Preliminary Design and Status of a Hydrazine MilliNewton Thruster Development," *AIAA,* 1999.

[17] N. Demmons, "ST-7-DRS Mission Colloid Thruster Development," *AIAA,* 2008.

[18] NASA-JPL, "Electric Propulsion," [Online]. Available: http://sec353ext.jpl.nasa.gov/ep/multimedia.html. [Accessed 7 5 2014].

[19] Texas Instruments, "LM25037 | PWM and Resonant Controllers," [Online]. Available: http://www.ti.com/product/lm25037. [Accessed 1 1 2014].